MNRAS **in press**, 1–17 (2017) Preprint 9 February 2017 Compiled using MNRAS LATEX style file v3.0

The Fan Region at 1.5 GHz. I: Polarized synchrotron emission extending beyond the Perseus Arm

A. S. Hill,[1,2⋆] T. L. Landecker,[3] E. Carretti,[1,4] K. Douglas,[5] X. H. Sun,[6] B. M. Gaensler,[6,7] S. A. Mao,[8] N. M. McClure-Griffiths,[1,9] W. Reich,[8] M. Wolleben,[10] J. M. Dickey,[11] A. D. Gray,[3] M. Haverkorn,[12] J. P. Leahy,[13] and D. H. F. M. Schnitzeler[8]

[1] *CSIRO Astronomy & Space Science, PO Box 76, Epping, NSW 1710, Australia*
[2] *Department of Astronomy, Haverford College, Haverford, PA 19041, USA*
[3] *National Research Council Canada, Herzberg Program in Astronomy and Astrophysics, Dominion Radio Astrophysical Observatory, PO Box 248, Penticton, British Columbia V2A 6J9, Canada*
[4] *Present address: INAF/Osservatorio Astronomico di Cagliari, Via della Scienza 5, I-09047 Selargius, Italy*
[5] *Physics and Astronomy Department, Okanagan College, 1000 KLO Road, Kelowna, British Columbia V1Y 4X8, Canada*
[6] *Sydney Institute for Astronomy, School of Physics, University of Sydney, NSW 2006, Australia*
[7] *Dunlap Institute for Astronomy and Astrophysics, University of Toronto, 50 St. George Street, Toronto, Ontario M5S 3H4, Canada*
[8] *Max-Planck-Institut für Radioastronomie, Auf dem Hügel 69, D-53121, Bonn, Germany*
[9] *Research School of Astronomy and Astrophysics, Australian National University, Canberra, ACT 2611, Australia*
[10] *Skaha Remote Sensing, 3165 Juniper Drive, Naramata, BC V0H 1N0, Canada*
[11] *University of Tasmania, School of Mathematics and Physics, Hobart, TAS 7001, Australia*
[12] *Department of Astrophysics/IMAPP, Radboud University Nijmegen, PO Box 9010, NL-6500 GL, Nijmegen, the Netherlands*
[13] *Jodrell Bank Centre for Astrophysics, Alan Turing Building, School of Physics and Astronomy, University of Manchester, Oxford Road, Manchester M13 9PL, UK*

arXiv:1702.02200v1 [astro-ph.GA] 7 Feb 2017

Accepted XXX. Received YYY; in original form ZZZ

ABSTRACT

The Fan Region is one of the dominant features in the polarized radio sky, long thought to be a local (distance $\lesssim$ 500 pc) synchrotron feature. We present $1.3 - 1.8$ GHz polarized radio continuum observations of the region from the Global Magneto-Ionic Medium Survey (GMIMS) and compare them to maps of Hα and polarized radio continuum intensity from $0.408 - 353$ GHz. The high-frequency (> 1 GHz) and low-frequency ($\lesssim$ 600 MHz) emission have different morphologies, suggesting a different physical origin. Portions of the 1.5 GHz Fan Region emission are depolarized by $\approx 30\%$ by ionized gas structures in the Perseus Arm, indicating that this fraction of the emission originates $\gtrapprox 2$ kpc away. We argue for the same conclusion based on the high polarization fraction at 1.5 GHz ($\approx 40\%$). The Fan Region is offset with respect to the Galactic plane, covering $-5^\circ \lesssim b \lesssim +10^\circ$; we attribute this offset to the warp in the outer Galaxy. We discuss origins of the polarized emission, including the spiral Galactic magnetic field. This idea is a plausible contributing factor although no model to date readily reproduces all of the observations. We conclude that models of the Galactic magnetic field should account for the $\gtrsim 1$ GHz emission from the Fan Region as a Galactic-scale, not purely local, feature.

Key words: Galaxy: structure – ISM: magnetic fields – ISM: structure – polarization – radio continuum: ISM

1 INTRODUCTION

Linearly polarized radio continuum emission arises from the interaction of ultrarelativistic electrons with a magnetic field. The first detections of polarized emission from the Galaxy (Westerhout et al. 1962; Wielebinski et al. 1962) already recognized the two large features that dominate the northern polarized sky, the North Polar Spur and the Fan Region. The Fan Region extends over a $\sim 60^\circ \times 30^\circ$ region, centred at Galactic longitude $\ell \approx 130^\circ$ slightly above the Galactic plane at Galactic latitude $b \approx +5^\circ$. The Fan Region is remarkable for the intensity of its polarized radiation

⋆ Email: ashill@haverford.edu

© 2017 The Authors

and the regularity of its polarization angle. In total intensity images, it does not stand out from its surroundings. It is identified by (and named for) electric field vectors which appear to fan out from the Galactic plane near $\ell = 130^\circ$ at low frequencies $\nu \lesssim 600$ MHz (Bingham & Shakeshaft 1967; Brouw & Spoelstra 1976). Polarized emission in this region of the sky is evident from ≈ 100 MHz (Iacobelli et al. 2013a) to 353 GHz (Planck Collaboration XIX 2015). All of this emission is generally referred to as the Fan Region.

The origin of the Fan Region is unknown, but most authors have considered it a local ($d \lesssim 500$ pc) feature (Wilkinson & Smith 1974; Spoelstra 1984). Verschuur (1968) identified a depolarized ring feature at 408 MHz at $(137^\circ, +7^\circ)$[1] which they associated with a star $140 - 200$ pc from the Sun to establish a lower limit to the distance; Iacobelli et al. (2013a) placed this ring ≈ 200 pc away based on $150 - 350$ MHz observations. Wilkinson & Smith (1974) found no depolarization at $\nu \leq 610$ MHz due to the H II region Sh2-202, establishing an upper limit. The modern distance to Sh2-202 is 0.97 ± 0.08 kpc (Foster & Brunt 2015). These arguments for a local origin of the Fan Region are based primarily on low-frequency observations. In contrast, Bingham & Shakeshaft (1967) argued that the high polarization fraction at 1407 MHz can only be produced by Galactic structure. Wolleben (2005) found depolarization by numerous H II regions and argued that the 1.4 GHz emission occurs over a range of distances from ≈ 500 pc to a few kpc, a range which includes both local gas and the Perseus spiral arm. Because the intrinsic polarization angle of synchrotron radiation is related to the orientation on the sky of the magnetic field in the emitting region, if the Fan Region emission originates over this long path length, it must indicate a uniform Galactic magnetic field on kpc scales in this direction (Wolleben et al. 2006).

In this paper, we present 1.5 GHz polarized continuum observations of the Fan Region. Our focus here is on morphological comparisons between continuum observations from 0.4 to 353 GHz and with spectroscopically-resolved Hα observations. We present our data in Section 2, briefly reviewing relevant depolarization mechanisms in Section 2.3. We discuss the kinematic features seen in Hα and H I observations in the direction of the Fan Region as they relate to Galactic structure in Section 3. We describe the Fan Region at all wavelengths and compare the morphology to observations of interstellar medium (ISM) structures with known distances in Section 4. In Section 5.1, we discuss the implications of the high observed fractional polarization in the Fan Region. In Sections 5.2 and 5.3, we construct a simple model of the synchrotron emission due to Galactic spiral structure, incorporating the effects of geometrical and depth depolarization, and compare the results to the observed synchrotron intensity as a function of longitude. We summarize the paper and draw conclusions in Section 6. In Paper II (A. S. Hill et al in prep), we will model depolarization due to Faraday effects in the Fan Region.

[1] We denote positions in Galactic coordinates as (ℓ, b).

2 OBSERVATIONS

2.1 GMIMS survey

We use radio polarization data from the Global Magneto-Ionic Medium Survey (GMIMS) high-band north (GMIMS-HBN). In GMIMS (Wolleben et al. 2009), we are using telescopes around the world to map polarized emission from the entire sky, north and south, spanning 300 to 1800 MHz. The survey is designed to measure the polarized intensity, $L(\phi)$, as a function of Faraday depth

$$\phi(s) = K \int_s^{\text{observer}} n_e(s')\, \mathbf{B}(s') \cdot d\mathbf{s}'. \quad (1)$$

Here $K \equiv e^3/(2\pi m_e^2 c^4) = 0.81\,(\text{cm}^{-3}\,\mu\text{G pc})^{-1}$ rad m^{-2}, n_e is the electron density in the intervening ISM, and $\mathbf{B}$ is the magnetic field. We acquire data in thousands of frequency channels to allow us to use rotation measure (RM) synthesis (Brentjens & de Bruyn 2005).

The GMIMS-HBN data were acquired with the 26 m John A. Galt Telescope at the Dominion Radio Astrophysical Observatory (DRAO) with continuous frequency coverage from 1280 to 1750 MHz. Data were acquired in 2048 individual channels of width 236.8 kHz. Wolleben et al. (2010b) describe the receiver and the data acquisition process for GMIMS-HBN, and Wolleben et al. (2010a) and Sun et al. (2015) give examples of use of GMIMS-HBN data. The full survey will be presented and publicly released elsewhere.

The observations were made by moving the telescope slowly up and down the meridian as the sky moved by; each such telescope track is referred to as a "scan". Earth rotation during a scan caused each scan to follow a diagonal track across the equatorial coordinate grid. Successive up and down scans were made until the sky was fully sampled between declinations -30° and $+87^\circ$. After calibration, the many scan crossings were reconciled using the "basketweaving" technique (Wolleben et al. 2010a), which we used to iteratively deduce the best-fit zero level for each scan. This process strips the sky minimum, which makes the zero point for Stokes I measurements inconsistent (Wolleben et al. 2010a), so we do not use total intensity data from GMIMS-HBN. Observations were made between sunset and sunrise to avoid contamination through sidelobes by radio emission from the Sun. The angular resolution varies from $40'$ to $30'$ across this frequency range; we have smoothed the data to a common resolution of $40'$ and reprojected to a plate carrée projection (Calabretta & Greisen 2002).

Daily calibration observations were made of the bright small-diameter sources Cas A, Cyg A, Tau A, and Vir A. Using flux densities and spectral indices of these sources from Baars et al. (1977), we converted the scan data to units of Janskys. The conversion factor from Janksys to Kelvins of main beam antenna temperature (equivalent to the gain of the telescope) was established from careful measurement of the antenna temperature produced by Cyg A on an absolute temperature scale established with resistive terminations at liquid nitrogen temperature and at $\approx 100^\circ$ C. Finally, data were converted to main-beam brightness temperatures by dividing by the beam efficiency of the telescope. We consider the temperature scale to be correct within $\sim 3\%$. Du et al. (2016) present details of the determination of telescope gain.

The Stokes Q and U spectra are smooth and there is no evidence of bandwidth depolarization in individual channels.

Sun et al. (2015) made tests of data quality from the GMIMS data in the vicinity of the North Polar Spur, another region of bright polarized emission. They concluded that the data set is of high quality in regions of bright polarized emission.

We apply RM synthesis to our polarization data cubes. In RM synthesis, we construct the Faraday dispersion function, which takes the form of a Fourier transform of the observed complex polarization vector, $\mathcal{P} = Q + iU$. The Faraday dispersion function is integrated over the interference-free portions of the observed band. At a given Faraday depth, RM synthesis accounts for rotation in the polarization angle over the band. Due to Faraday rotation, there is no single polarization angle which describes the data at all frequencies in the band. Without RM synthesis, integrating over many channels would lead to significant bandwidth depolarization (e.g. Brentjens & de Bruyn 2005; Heald 2009; Schnitzeler et al. 2009).

RM synthesis also allows us to separate the emission as a function of ϕ. For each pixel on the sky, we construct the polarized intensity $L_{1.5}(\phi)$ sampled every 5 rad m^{-2}. Our observing frequencies and spectral resolution leave us sensitive to emission with $|\phi| < 2 \times 10^5$ rad m^{-2}; the resolution is $\delta\phi = 149$ rad m^{-2} (calculated following Schnitzeler et al. 2009). The data were recorded and Faraday depth spectra calculated in equatorial coordinates; we subsequently reprojected to Galactic coordinates. From each Faraday depth spectrum, we calculated the peak polarized intensity at each pixel using a three-point quadratic fit with the `miriad` task `moment`. The polarized intensity images we present in this paper are images of this peak polarized intensity. The Faraday depth of the peak is typically at $|\phi| < 10$ rad m^{-2}, so these images are similar to an image of the $\phi = 0$ rad m^{-2} channel. With the large $\delta\phi$, we assume that there is only a single component resolved by the GMIMS-HBN observations.

When all of the polarized signal is at a single Faraday depth, an image produced with RM synthesis has the noise expected from the entire band rather than the noise from individual frequency channels. The noise in each ϕ channel is $\sigma_L \approx 0.02$ K, making the signal-to-noise ratio in the Fan Region $\gtrsim 20$ on a single-pixel basis. This allows us to measure the centroid of Faraday depth components with an uncertainty of ≈ 3 rad m^{-2} in the Fan Region. The structures in Faraday depth in the Fan Region seen in low-frequency observations are typically $\sim 1-10$ rad m^{-2} in extent (Iacobelli et al. 2013b), so we do not resolve multiple Faraday depth components with the GMIMS-HBN data; a future low-frequency component of the GMIMS survey will enable the separation of these narrow Faraday depth components. With a maximum frequency of 1750 MHz, we are not sensitive to individual Faraday depth features which are wider than ≈ 107 rad m^{-2} (Brentjens & de Bruyn 2005).

Wolleben et al. (2006) presented an absolutely-calibrated 1.4 GHz polarization survey also using John A. Galt Telescope observations. This older survey employed a single channel of bandwidth 12 MHz and a drift scanning strategy. Each drift scan was Nyquist-sampled in right ascension but the survey achieved 41.7% of Nyquist sampling in declination. The GMIMS-HBN survey improves upon the Wolleben et al. (2006) survey with a much wider bandwidth and full Nyquist sampling. Moreover, with the basketweaving observing strategy, each point is observed twice, reducing uncertainty relative to the drift scan strategy.

2.2 Complementary data sets

In addition to the GMIMS data presented here, we use several published data sets which provide complementary information. To trace synchrotron emission adequately, we have chosen data sets at a range of frequencies because depolarization cannot be understood from one frequency alone. We have also chosen data sets which trace the dust and ionized and neutral gas (with spectral resolution allowing separation of emission due to Galactic rotation) in the diffuse ISM. We have regridded all of the data sets to a plate carrée projection image with 0.5° pixels. We list frequencies, bandwidths, beam sizes, sampling, and the coverage as is relevant to the Fan Region of each of these surveys in Table 1. We refer the reader to the references in Table 1 for details but mention the most important points for our work here.

We use spectroscopic maps of Hα emission from data release 1 of the all-sky Wisconsin H-Alpha Mapper Sky Survey (WHAM-SS)[2] and of H I emission from the Leiden-Argentine-Bonn (LAB) survey. We use the low-frequency continuum surveys of Brouw & Spoelstra (1976), compiled and resampled on a regularly gridded map by Carretti et al. (2005). These observations used rotating feed antennas and thus record the polarized intensity and polarization angle directly (Berkhuijsen et al. 1964). Especially at the higher frequencies, these data are severely undersampled (see Table 1). We use 23 GHz data from the nine-year data release of the *WMAP* experiment. The high frequency makes these data virtually free from Faraday rotation effects, either angle rotation or depolarization. For the Urumqi 4.8 GHz observations, Gao et al. (2010) set the zero level by extrapolating the WMAP 23 GHz data using a spectral index measured from 23 GHz (WMAP) to 1.4 GHz (Wolleben et al. 2006). This assumes that there is little Faraday depolarization across the band (Sun et al. 2007), an assumption supported by consistent spectral indices. However, the Wolleben et al. (2006) data do not show the depolarization effects that are evident in the GMIMS-HBN data presented here (see § 4.1 below). If there is any Faraday depolarization at 4.8 GHz on scales larger than a few degrees (where the scaled 23 GHz data sets the zero level), the Urumqi 4.8 GHz data would not be sensitive to it.

In the 353 GHz image from the *Planck* mission, the thermal emission from dust dominates over other contributions, and the polarization of the signal traces the Galactic magnetic field (Planck Collaboration XIX 2015). The Canadian Galactic Plane Survey (CGPS) provides high angular resolution polarized radio continuum data at 1420 MHz for a small portion of the Fan region using the DRAO Synthesis Telescope. The Wolleben et al. (2006) data provide information on the largest angular scales for the CGPS data; Effelsberg 100 m Telescope data provide information on intermediate scales.

2.3 Synchroton emission and depolarization

The polarized radio continuum emission we present in this paper is primarily due to synchrotron emission and, at 353 GHz, dust emission. As polarized radiation propagates

[2] `http://www.astro.wisc.edu/wham/`

Table 1. Data sets used. Bandwidths and channel widths are listed in frequency units for continuum surveys and velocity units for spectral line surveys. The sampling column lists the approximate typical beam spacing on the sky in the midplane for surveys which are not Nyquist sampled. *References*: Dwingeloo: Brouw & Spoelstra (1976); Carretti et al. (2005). Stockert/Villa Elisa: Reich (1982); Reich & Reich (1986); Reich et al. (2001). CGPS: Taylor et al. (2003); Landecker et al. (2010). LAB: Kalberla et al. (2005). GMIMS-HBN: This work. Urumqi: Gao et al. (2010). *WMAP*: Bennett et al. (2013). *Planck*: Tauber et al. (2010); Planck Collaboration I (2016). WHAM-SS: Haffner et al. (2003, 2010).

Survey	Stokes/ Line	Frequency/ Wavelength	Bandwidth	Channel width	Beam FWHM	Sampling	Coverage
Dwingeloo	Q, U	408 MHz	2 MHz	2 MHz	2.3°	2.3° (irregular)	Northern sky
Dwingeloo	Q, U	465 MHz	2 MHz	2 MHz	2.0°	2.3° (irregular)	Northern sky
Dwingeloo	Q, U	610 MHz	4 MHz	4 MHz	1.5°	2.3° (irregular)	Northern sky
Dwingeloo	Q, U	820 MHz	4 MHz	4 MHz	1.0°	2.3° (irregular)	Northern sky
Dwingeloo	Q, U	1411 MHz	7 MHz	7 MHz	0.6°	2.3° (irregular)	Northern sky
Stockert/Villa Elisa	I	1420 MHz	18 MHz	18 MHz	0.6°	Nyquist	All sky
CGPS	I, Q, U	1420 MHz	35 MHz	35 MHz	0.02°	Nyquist	$-3° < b < +5°$
LAB	H I	1421 MHz	± 400 km s^{-1}	1 km s^{-1}	0.6°	0.5°	All sky
GMIMS-HBN	Q, U	1500 MHz	470 MHz	0.2 MHz	0.6°	Nyquist	$-30° < \delta < +87°$
Urumqi	I, Q, U	4800 MHz	600 MHz	600 MHz	0.16°	Nyquist	W4 superbubble
WMAP	I, Q, U	22.8 GHz	5.5 GHz	5.5 GHz	0.82°	Nyquist	All sky
Planck	I, Q, U	353 GHz	116 GHz	116 GHz	0.08°	Nyquist	All sky
WHAM-SS	Hα	656.3 nm	± 80 km s^{-1}	12 km s^{-1}	1.0°	1.0°	All sky

through the ionized ISM, depolarization effects reduce the polarized intensity by producing polarization vectors at different angles either along the line of sight or within the beam. The superposition of these vectors reduces the observed polarized intensity (Burn 1966; Tribble 1991; Sokoloff et al. 1998; Gaensler et al. 2001). *Beam depolarization* arises when different paths within the beam have different Faraday depths (see eq. 1) and thus polarization angles. Foreground turbulent regions can lead to significant beam depolarization. *Depth depolarization* occurs when distant emission is Faraday-rotated and cancels more local emission. Depth depolarization generally refers to an effect that occurs over a long path. Faraday screens can rotate background Faraday rotation and cause depolarization in a similar manner but over a very short path (Sun et al. 2007); we refer to this as *Faraday screen depolarization*. These three effects are results of Faraday rotation and are thus frequency-dependent. *Geometrical depolarization* is the product of different orientations of the magnetic field at different distances along the line of sight resulting in the superposition of emission with different intrinsic polarization angles (Miville-Deschênes et al. 2008; Delabrouille et al. 2013). Geometrical depolarization is the most important depolarization mechanism at high frequencies. At 23 GHz, the change in polarization angle $\Delta\psi \approx 0.01$ rad for $\phi = 50$ rad m^{-2}), so Faraday rotation is negligible.

3 KINEMATIC FEATURES AND DISTANCES

Because all components of the ISM (atomic, molecular, and ionized gas as well as the magnetic field) are inter-related, we examine the role of Galactic structure in producing both the ionized gas and the polarized emission from the Fan Region. In this section, we review our knowledge of Galactic structure and the distances to observed features in the second and third quadrants of the Galaxy.

Sightlines towards the Fan Region ($\ell \approx 130°$) pass through the Perseus and outer spiral arms. We illustrate this with an overhead view of the Galaxy in Figure 1. The Perseus Arm, which Benjamin (2008) considers one of two "major" spiral arms, is observed in ionized and neutral gas and star formation. It is about 2 kpc away at a Galactocentric radius of ≈ 10 kpc, while the Outer Arm, likely a more minor arm with a concentration of gas but not of old stars, is ≈ 6 kpc away at a Galactocentric radius of ≈ 13 kpc (e.g. Xu et al. 2006; Churchwell et al. 2009; Reid et al. 2014).

In the second quadrant, sightlines are closer to normal to these spiral arms than are similar sightlines in the third quadrant. As an example, we consider the two sightlines 50° from the anticentre ($\ell = 180°$), $\ell = 130°$ and $\ell = 230°$. These are shown as dashed lines in Figure 1. One might expect these sightlines to probe similar parts of the Galaxy. The angle between the $\ell = 230°$ sightline and the normal to the Perseus Arm is $\approx 45°$, whereas the angle between the $\ell = 130°$ sightline and the Perseus Arm normal is $\approx 30°$. For the outer arm, the offset between the $\ell = 130°$ sightline and the normal to the arm is $\approx 15°$; the $\ell \approx 230°$ sightline does not intersect any known Outer Arm material. If the Outer Arm continued at the same pitch angle, the $\ell = 230°$ sightline would encounter the Outer Arm much further out, > 20 kpc from the Galactic Centre.

In Figure 2, we plot longitude-velocity diagrams of H I and Hα to describe the structure of Galactic emission in this region. The Perseus Arm is the dominant feature, with the H I and Hα emission brightest at $V_{\rm LSR} \approx -50$ km s^{-1} in the midplane at $\ell = 135°$. There are kinematically-distinct H I components at local and Perseus Arm velocities. Because the brightest Hα emission is concentrated in H II regions, the Hα is patchier than the H I. Typical Hα line widths are ≈ 30 km s^{-1}, compared to 10 km s^{-1} for H I, which also makes it more difficult to separate Hα components. However, the local and Perseus Arm Hα components are kinematically distinct at $150° \gtrsim \ell \gtrsim 130°$ (Haffner et al. 1999), and Figure 2 shows distinct components at $V_{\rm LSR} \approx -50$ km s^{-1} and $V_{\rm LSR} \approx -10$ km s^{-1} extending to $\ell \approx 100°$. We adopt

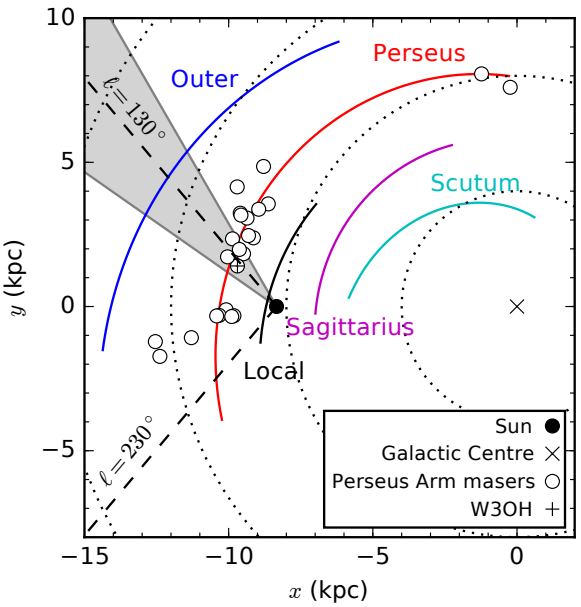

Figure 1. View of the Galaxy from above with spiral arms from Reid et al. (2014). The longitude range $120° < \ell < 145°$, the region which contains the brightest emission from the Fan Region, is shaded gray.

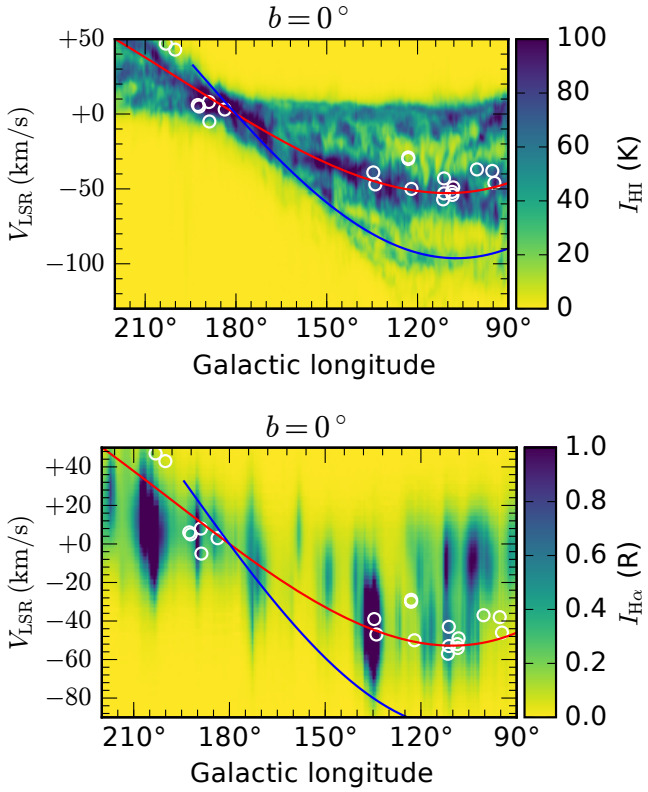

Figure 2. Longitude-velocity diagrams of H I from LAB (top) and Hα from WHAM (bottom). White circles show the longitudes and velocities of masers in the Perseus Arm from Reid et al. (2014), as in Fig. 1. Red and blue lines show the Perseus and Outer arms, respectively (see text).

-75 km s^{-1} $< V_{\rm LSR} < -30$ km s^{-1} as the velocity range which defines the Perseus Arm Hα.

The distance to masers in the Perseus Arm ranges from 1.9 to 2.8 kpc over $120° < \ell < 145°$ with a line-of-sight depth of 0.38 kpc from parallax measurements (Reid et al. 2009, 2014, and references therein). We show the longitudes and velocities of the masers Reid et al. used to determine this distance in Figure 2. The maser positions and velocities trace both the Hα and H I emission. We also plot lines showing the longitude and velocity of the Perseus and Outer arms with velocities derived using the linear function defining the Galactic rotation speed from Reid et al. (2014, their Bayesian fit D1). Because kinematic distances in the second quadrant overestimate the true source distance measured by parallax (Foster & MacWilliams 2006; Reid et al. 2009) and the purpose of these lines is simply to guide the eye, we multiplied the derived velocities for the arms by 1.5 and 1.3, respectively, to match the lines to the kinematic features.

The latitude-velocity diagram in Figure 3 shows the warp in the Fan Region. There is evidence of a warp in the further reaches of the Perseus Arm: the bright emission at $V_{\rm LSR} \approx -45$ km s^{-1} is centred at $b = 0°$ but gas at more negative velocities predominantly lies above $b = 0°$. At $V_{\rm LSR} \approx -75$ km s^{-1}, the warp is evident at $b \approx +3°$. This is the Outer Arm, at a distance of ≈ 6 kpc (Hachisuka et al. 2009; Reid et al. 2014). At $V_{\rm LSR} \approx -100$ km s^{-1}, the H I emission from the warp is brightest at $b \approx +6°$, while it extends to $b = +8°$ at $V_{\rm LSR} \approx -115$ km s^{-1}. In this region, there is H I emission near $b = 0°$ out to large velocities in addition to the warped emission.

In Figure 3, we also show a fit to the warp along a sightline in the Fan Region, calculating following Kalberla et al. (2007, with data provided by P. M. W. Kalberla, private communication, 2016). In this fit, the emission is centred near $b = +3°$ from 1 kpc $\lesssim D \lesssim$ 5 kpc, near $b = +5.5°$ from 8 kpc $\lesssim D \lesssim$ 15 kpc, and near $b = +9°$ over $D \gtrsim 20$ kpc. The emission at Perseus Arm velocities around $\ell = 130°$ is centred near $b = +1°$, while emission at Outer Arm velocities in this region is centred near $b = +3°$ at a distance of 6 kpc (Hachisuka et al. 2009; Reid et al. 2014).

There is no clear evidence of a warp in Hα emission, likely due to four factors: 1) the broader line widths of Hα ($\approx 30 - 40$ km s^{-1}, evident in Fig. 2) make it difficult to separate the Outer Arm from the Perseus Arm in Hα; 2) extinction makes distant Hα more difficult to observe (Madsen & Reynolds 2005); 3) the scale height of the warm ionized medium (WIM) is large enough ($1 - 1.4$ kpc; Haffner et al. 1999; Gaensler et al. 2008; Savage & Wakker 2009; Schnitzeler 2012) that a 3° offset of the midplane is a relatively small effect; and 4) the star formation rate in the Outer Arm may be lower because star formation rates are typically lower further from the Galactic Centre (Kennicutt & Evans 2012), producing a lower ionizing flux and thus less Hα emission.

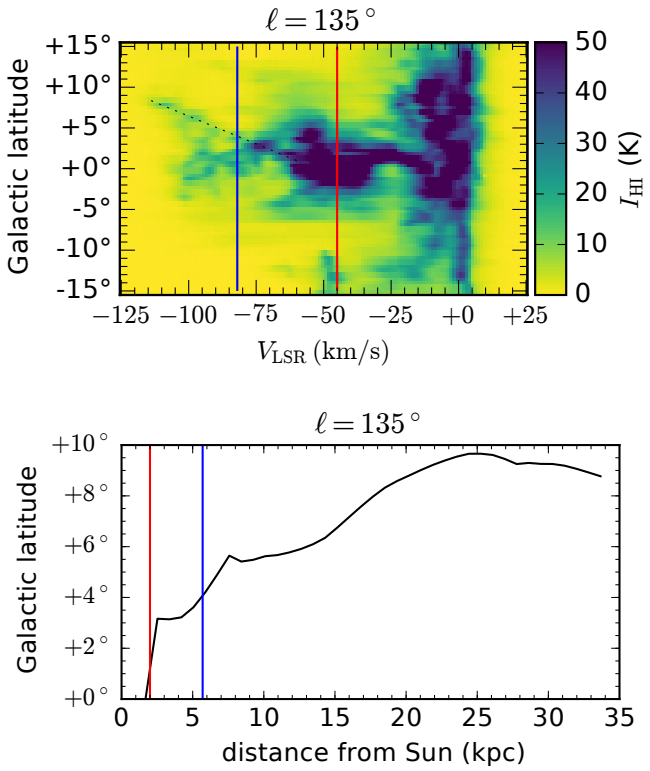

Figure 3. *Top:* Latitude-velocity diagram of H I from LAB. The velocities of the Perseus (red) and Outer (blue) arms at this longitude as shown in Fig. 2 are shown. A dotted line indicates the approximate position of the warp emission. *Bottom:* Latitude of the midplane of the warped Galaxy as a function of distance from the Sun calculated using the fit to the LAB data determined by Kalberla et al. (2007). For a discussion of the considerable uncertainties in this plot, see their paper. Distances to the arms at $\ell = 135°$ from the fit to maser distances (Reid et al. 2014) are shown as an indication, but the systematic uncertainties in the kinematic distances used to determine the latitude of the warp are large.

4 RESULTS

4.1 Morphology of polarized emission

In Figure 4 we show the Fan Region in its Galactic context. The all-sky images are centred on the second quadrant ($90° \lesssim \ell \lesssim 180°$), where the Fan Region is located. The Fan Region is identified by the bright signal in polarized intensity at 1.5 GHz ($L_{1.5}$), 23 GHz (L_{23}), and 353 GHz (L_{353}). At 1.5 GHz, the polarized emission is centred above the plane, with $L_{1.5} \gtrsim 0.1$ K (green in Fig. 4) emission extending over $-12° \lesssim b \lesssim +25°$, $90° \lesssim \ell \lesssim 180°$. The 23 GHz and 353 GHz emission are roughly similar, in both cases with emission centred at $b \approx +4°$.

The brightest emission, $L_{1.5} \gtrsim 0.3$ K, is mostly in a smaller region, $120° < \ell < 150°$ and $-6° < b < +12°$. We show maps of polarized intensity in this region from 408 MHz − 23 GHz in Figure 5. The morphology is qualitatively different at $\nu \lesssim 600$ MHz and $\nu \gtrsim 1$ GHz. At high frequencies, the emission fills most of this region. At 23 GHz, the emission is bright both at $|b| \lesssim 2°$ and above the plane up to $+10°$. In contrast, at 1.5 GHz and all lower frequencies, the emission is much fainter in the plane ($|b| \lesssim 2°$) than at $b \approx +8°$. However, the bright emission is similar in morphology at 23 and 1.5 GHz at $b \gtrsim +3°$. At both frequencies, the bright emission follows an arc from around $(134°, +8°)$ to $(128°, +3°)$, emphasized by the yellow contours in Figure 5.

There is no obvious feature corresponding to the Fan Region in total intensity at 1.4 GHz. We show the polarization fraction at ∼ 1.5 GHz in Figure 6. The structure of the polarization fraction image closely traces that of the polarized intensity image (Fig. 5*b*) because the Stokes I emission is much more uniform than the polarized intensity. The polarization fraction is highest, ≈ 40%, in the region where $L_{1.5}$ is brightest, in the arc which peaks at $(134°, +8°)$.

There is a patch where the polarized intensity at 1.5 GHz is lower, centred at $(134.5°, +4°)$ and $\approx 5°$ in diameter; this area, shown with black circles in Figures 5–7 as well as Figures 11–12 below, is a major focus of this paper. The reduced $L_{1.5}$ cannot be entirely due to Faraday depolarization because it is also seen to some extent in L_{23}. However, the 1.5 GHz fractional polarization in Figure 6 is lower in that patch (≈ 30%) than in the surrounding Fan Region (≈ 40%).

This reduction in polarized intensity is not seen in the Dwingeloo 1411 MHz data (Brouw & Spoelstra 1976; Carretti et al. 2005). That survey is sparsely sampled, and by checking the measured data points we have verified that there was no measurement near $(134.5°, +4°)$: the 1411 MHz survey could not have detected this feature. A similar check of the 820 MHz observation points shows that there was a measurement close to this position, and the interpolated image at 820 MHz does indeed show a decline in polarized intensity at this position (Figure 5*c*).

Somewhat puzzling is the fact that the depression in polarized intensity is not seen in the Wolleben et al. (2006) data. That survey was made using drift scans, and a check showed that drift scans were made across this region at full sampling; however, no cross scans in declination were made. We regard the GMIMS data as more reliable. Scanning was in two directions, fully Nyquist sampled, and the area of interest was crossed by many scans. The intersecting scans were reconciled by the basketweaving technique. Inspection of the GMIMS datacube shows that the depression in polarized intensity is seen at every frequency across the GMIMS band as well as in the image after RM synthesis.

At the lowest frequencies, the polarized emission is brightest in a ring centred at $(137°, +8°)$, shown with blue circles in Figure 5. At 150 − 350 MHz, this ring is the dominant feature identifiable in the Fan Region, with a diameter of about 7° in Westerbork Synthesis Radio Telescope data. Various authors have used Westerbork data to describe the ring as a relic Strömgren sphere at a distance of ≈ 200 pc (Iacobelli et al. 2013a) and as a depolarization artefact of a uniform Faraday depth distribution (Haverkorn et al. 2003). The Westerbork data use aperture synthesis and thus are not sensitive to features $\gtrsim 10°$ in size (Bernardi et al. 2009), whereas the Brouw & Spoelstra (1976) data are single-antenna and thus should be sensitive to emission on all resolved scales. The ring is also the dominant feature at frequencies up to 610 MHz (see Figure 5). Its diameter is larger at higher frequencies, and it also becomes less clearly

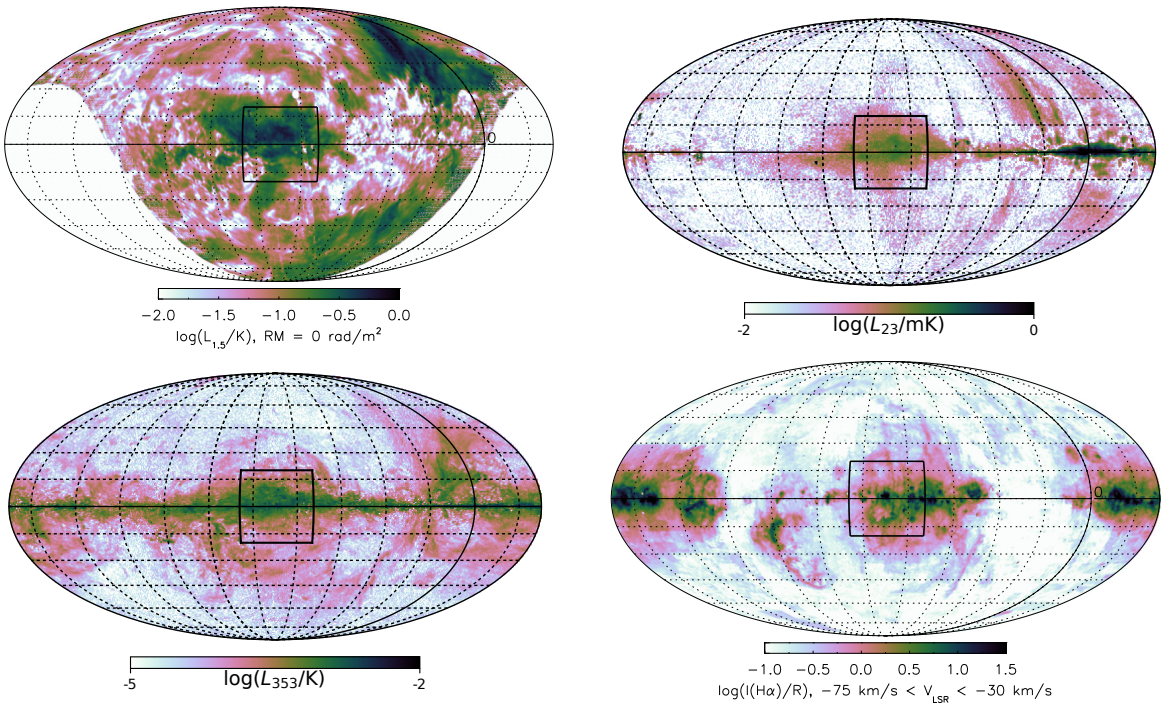

Figure 4. All-sky images centred on $\ell = 135°$ and $b = 0°$ in a Mollweide projection with grid lines every $\Delta\ell = 30°$, $\Delta b = 15°$. Solid lines show $\ell = 0°$ and $b = 0°$. The intensity scales in each image are logarithmic. Top left: GMIMS-HBN 1.5 GHz polarized intensity at Faraday depth 0 rad m^{-2}. Top right: WMAP 23 GHz linearly polarized intensity (Bennett et al. 2013). Bottom left: Planck 353 GHz linearly polarized intensity from the 2015 data release (Planck Collaboration I 2016) smoothed with a 20′ FWHM Gaussian beam. Bottom right: WHAM-SS Hα emission (Haffner et al. 2003, 2010) integrated over -75 km s$^{-1} < V_{\rm LSR} < -30$ km s^{-1}, isolating emission from the Perseus Arm and beyond. Boxes indicate the corners of the region shown in Fig. 5.

defined as a circular feature. At $\nu \gtrsim 1.5$ GHz, the ring is not apparent. At 820 MHz, both the ring and the broader, high-frequency feature are evident.

4.2 Morphological comparison of Hα and 1 − 23 GHz polarized emission

The lower-right panel of Figure 4 shows Hα emission with a velocity criterion (-75 km s$^{-1} < V_{\rm LSR} < -30$ km s^{-1}) which excludes local gas but includes emission from the Perseus Arm and more distant gas (Haffner et al. 1999; Madsen et al. 2006). We compare $L_{1.5}$ with Hα at the Perseus Arm velocity as well as at local velocities and integrated over all velocities in Figure 7. As in the polarized continuum maps, the Hα emission is brightest around $100° \lesssim \ell \lesssim 150°$, although the H$\alpha$ emission is centred at somewhat lower latitudes ($b \approx 0°$) and longitudes than the polarized continuum. The highest 1.5 GHz polarized intensity, $L_{1.5} \approx 0.65$ K, is in a region (near $(134°, +8°)$) with little Hα emission at any velocity. The region with depressed $L_{1.5}$ around $(134.5°, +4°)$ (which we introduced in Section 4.1) corresponds with increased Hα intensity at Perseus Arm velocities. The white ($I_{\rm H\alpha} = 2.0$ R[3]) contour in Fig. 7*c* traces the lower envelope of the bright ($L_{1.5} \gtrsim 0.5$ K; dark blue in Fig. 7*a*–*c*) polarized emission, suggesting qualitatively that the polarized intensity in this region is anti-correlated with the Perseus Arm Hα intensity.

We quantify the relationship between $L_{1.5}$ and $I_{\rm H\alpha}$ from the Perseus Arm in the scatter plot in Figure 8. We chose a narrow latitude range to minimize the impact of the latitude dependence of $I_{\rm H\alpha}$ on the scatter plot. The latitude range $+3° < b < +6°$ cuts through the region of reduced $L_{1.5}$ around $(134.5°, +4°)$ we discussed in Section 4.1. We chose the longitude range $128° < \ell < 140°$ to encompass the bright emission from the Fan Region as seen at 1.5 GHz, 23 GHz, and 353 GHz (see Figs. 4 and 5). In the six sightlines in the plot with $I_{\rm H\alpha} > 5$ R, the polarized intensity is very consistent, $\langle L_{1.5} \rangle = 0.44$ K with standard deviation $\sigma_{L1.5} = 0.02$ K. In sightlines with $I_{\rm H\alpha} < 3$ R, there is a wider range of polarized intensities, typically $\approx 30\%$ higher than in the Hα-bright sightlines. The anticorrelation of $L_{1.5}$ with $I_{\rm H\alpha}$ is most likely due to depolarization, not an intrinsic absence of polarized emission along these sightlines. We expect depolarization due to all gas in front of the emission, so correlating structures in depolarization with Hα emission at an estimated distance measures the minimum distance to the emitting gas. The Hα emission from the Perseus Arm (Fig. 7*c* and *f*) is brightest in a roughly circular region centred on the W3/W4/W5 complex of H II regions. (W4 is shown with a + sign in Fig. 7.) From the optical line ratios, this bright Hα emission is more typical of O star H II regions than of the diffuse WIM (Madsen et al. 2006), indicating that the gas is primarily photoionized by O stars in those H II regions. The arched shape of the 1.5 GHz emission is matched by an arch in the Perseus Arm Hα contour at $(134°, +7°)$ in Figure 7*c*. This fainter Hα from the Perseus

[3] 1 Rayleigh (R) $= 10^6/(4\pi)$ photons cm^{-2} s^{-1} sr^{-1}.

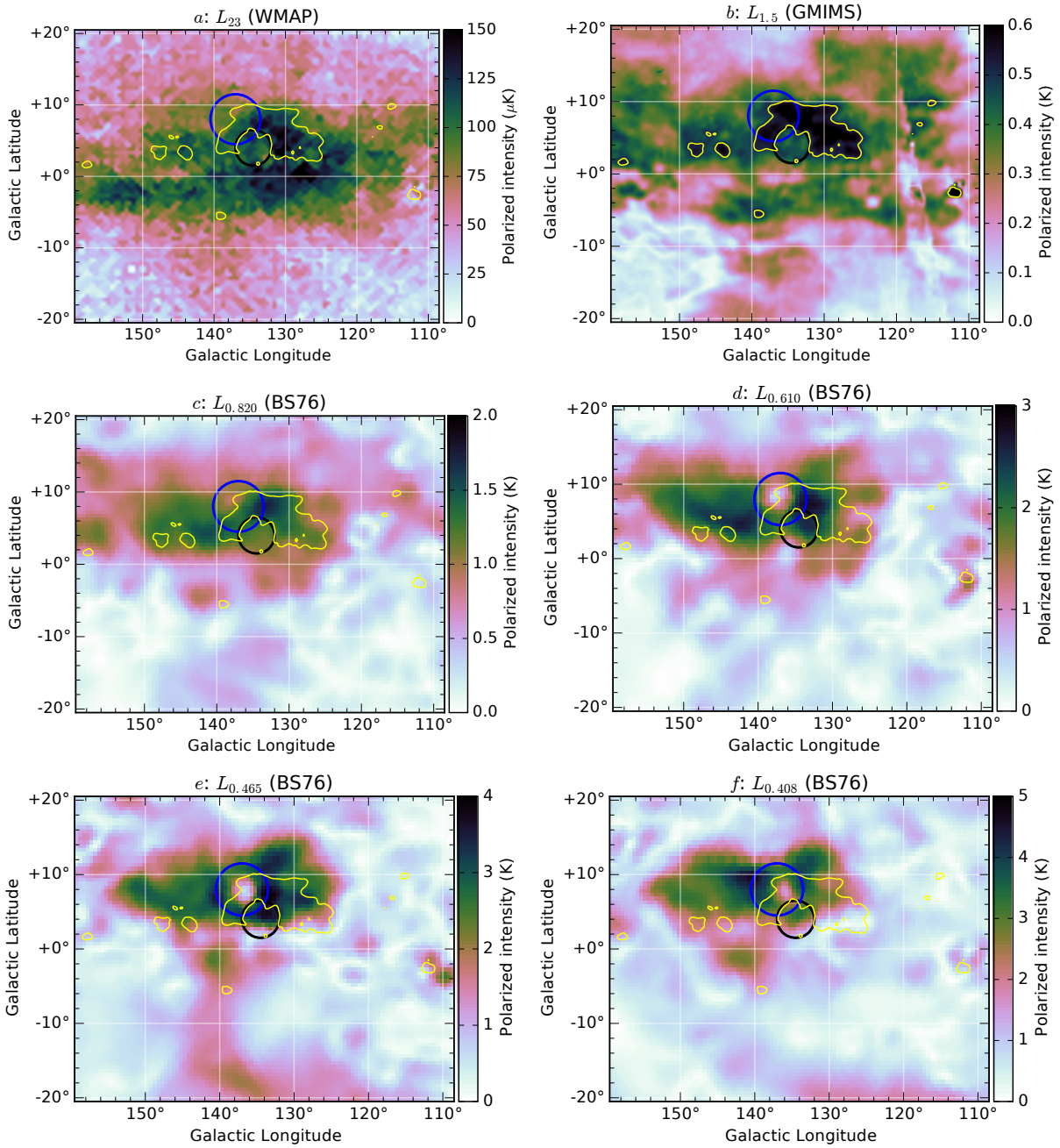

Figure 5. Images of polarized intensity at 23 GHz (WMAP), 1.5 GHz (GMIMS), and 408 − 820 MHz (Brouw & Spoelstra 1976; Carretti et al. 2005). Yellow contours show GMIMS data ($L_{1.5}$) at an antenna temperature of 0.5 K. Black and blue circles show the features at $(134.5°, +4°)$ and $(137°, +8°)$ discussed in the text. A small artefact remains in the GMIMS $L_{1.5}$ image at 0 hours right ascension (the diagonal stripe around $\ell = 115°$ in panel *b*).

Arm, which is spatially coincident with the high polarized intensity from the Fan Region, has optical line ratios (especially [N II]λ6584/Hα) which are higher and thus more WIM-like than the H II region emission (see Figure 11 of Madsen et al. 2006).

We have not applied an extinction correction to the Hα data. From a comparison of Hα and Hβ observations, there are $A_V = 3.13 \pm 0.2$ magnitudes of extinction towards the W4 H II region at Hα at $(134.7°, +0.9°)$, the brightest sightline in this region in Hα (Madsen et al. 2006). Robust extinction measurements are only available for a small number of individual sightlines, so a systematic extinction correction is difficult. We expect that the dust column and thus the extinction is highest in sightlines which are brightest in Hα, so we expect that the main impact of an extinction correction would be to increase the contrast between the faint sightlines and the bright ones. This would not change our interpretation of Figures 7 and 8: the sightlines with high $L_{1.5}$ would still be the sightlines with the lowest $I_{\mathrm{H}\alpha}$.

In Figure 9, we show a slice of 1.5 and 23 GHz polarized

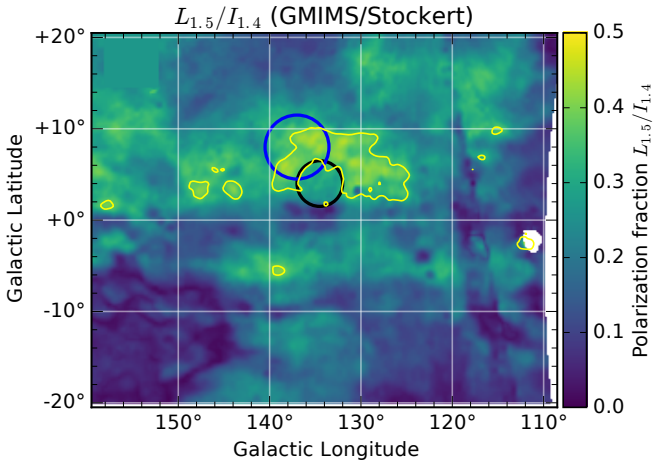

Figure 6. Polarization fraction from comparing the GMIMS data to the Stockert 1.4 GHz Stokes I data (Reich 1982). Yellow contours show $L_{1.5} = 0.5$ K, as in Fig. 5.

intensities and the Perseus Arm Hα intensity. In this slice, the Hα intensity peaks at $\ell = 134°$, the location of the minimum in $L_{1.5}$. At 1.5 GHz, the polarized intensity peaks at $\ell \approx 130°$ and 138°, areas of relatively low Hα intensity, and has a local minimum near $\ell = 134°$. A similar trend is evident at 820 MHz (not shown) but not at lower radio frequencies. This trend is also evident at 23 GHz, although the local maximum at $\ell = 138°$ is not present. The figure also shows the local Hα emission, which does not have a discernible peak either correlated or anti-correlated with the polarized intensity. This indicates that the depolarization is due to Hα-emitting gas at the velocity of the Perseus Arm.

The vertical profile in Figure 10 shows that the 1.5 GHz synchrotron intensity is highest at $b \approx +8°$, with no sign of a comparable enhancement at $b \approx -8°$. The 23 GHz polarized emission is relatively bright over the range $-5° \lesssim b \lesssim +10°$. The upper envelopes of $L_{1.5}$ and L_{23} around $b = +10°$ are similar. The 1.5 GHz intensity is much fainter at $b < +5°$, whereas the 23 GHz intensity is comparable at $b \approx 0°$ and $b = +8°$. We interpret this as the result of beam depolarization; $I_{\mathrm{H}\alpha} \approx 3 - 4$ R at $b = -5°$, compared to ≈ 1 R at corresponding latitudes above the plane. In our picture, the 23 GHz and 1.5 GHz emission each originate in the same volume. The 23 GHz polarized intensity traces the full extent of the synchrotron-emitting region without Faraday depolarization, while some of the 1.5 GHz emission is Faraday depolarized.

4.3 Using CGPS data to locate the Fan Region

High resolution data are less subject to beam depolarization than the GMIMS data. We use polarization data from the CGPS to obtain information relevant to the Fan Region at low latitudes, shown in Figure 11. In the vicinity of the Fan region the angular resolution is close to 1′. We also refer to Figures 5 – 7 of Landecker et al. (2010), which show images of total intensity and polarized intensity from the CGPS over $66° < \ell < 186°$.

The images show many areas of emisison that is structured on small angular scales. Virtually all of this emission is unrelated to objects seen in total intensity: these are typical Faraday screen structures.

The polarized intensity on and around W4 at $(134.7°, +0.9°)$ and W5 at $(137.6°, +1.1°)$, traced by $I_{1.4}$ (white) and Hα (black) contours in Figure 11, stands out from the highly structured surroundings. Toward these two H II regions there is a marked absence of small-scale structure. Along the southern perimeter of these H II regions, but offset from the edge, there is an abrupt transition to highly structured polarized emission. This can also be seen clearly in Figures 7 and 8 of West et al. (2007). Gray et al. (1999) showed that this transition below W4 is related to the H II region (and that is why the transition mirrors its shape): there is an extended, low-density ionized halo that extends beyond the boundaries defined by 1.5 GHz continuum imaging in total intensity; this halo is evident with the WHAM data we show in Figures 7 and 11 as well as in 2.7 GHz total intensity in Figure 7 of Gray et al. (1999). The gradient of Faraday rotation in that envelope is evidently sufficient to cause beam depolarization. The density of ionized gas drops off with distance beyond the H II region until the gradient of rotation is no longer sufficient to cause beam depolarization, and the small-scale structure re-appears.

Our conclusion is that most, and probably all, of this highly structured emission originates in the Perseus Arm, possibly in the vicinity of W4 and W5 which are on the near surface of the Arm but possibly further inside the Arm. The smoother emission seen towards W4 is more local emission. It is expected that structures in the local emission will have an angular scale that is larger than structures in the Perseus Arm.

There are two complications to this picture. First, the bright and compact source W3 at $(133.8°, +1.2°)$ creates imaging artefacts, seen as rings superimposed on W4. Second, there is a foreground object superimposed on W5, evident in Figure 11 as a pink ($L_{1.5} \approx 0.2$ K) ring at $(137.5°, +1.1°)$. Gray et al. (1998) demonstrate that this lens-like object is either an enhancement of magnetic field or, more likely, an enhancement of electron density, and conclude that it lies somewhere along the 2 kpc line of sight between W5 and the Sun.

Many H II regions other than W4 and W5 in the vicinity show similar behaviour: all of them depolarize distant emission, leaving only foreground polarized emission that has smooth structure (Landecker et al. 2010). This extends as far as $\ell = 173°$, where the same depolarization effect is seen against the G173+1.5 star formation complex in the Perseus Arm (distance 1.8 kpc; Kang et al. 2012).

The region LBN 0679 is a bright filament in total intensity that runs from $(141°, -1.5°)$ to $(140°, 0°)$. It is associated with H I at -40 ± 1.5 km s^{-1} (Green 1989). Other H II regions in the vicinity with similar velocities are at a distance around 0.7 kpc (Foster & Brunt 2015). LBN 0679 shows the same polarization signature: on the H II region the polarized intensity is smooth, while to either side it is highy structured.

It is evident from Figures 4 – 7, 10, and 11 that there is strong depolarization in the plane at 1.5 GHz. There is an area of depolarization extending over $128° < \ell < 140°, -1° < b < +2°$. In the CGPS data, the southern edge of this depolarization zone has a very sharp edge, barely

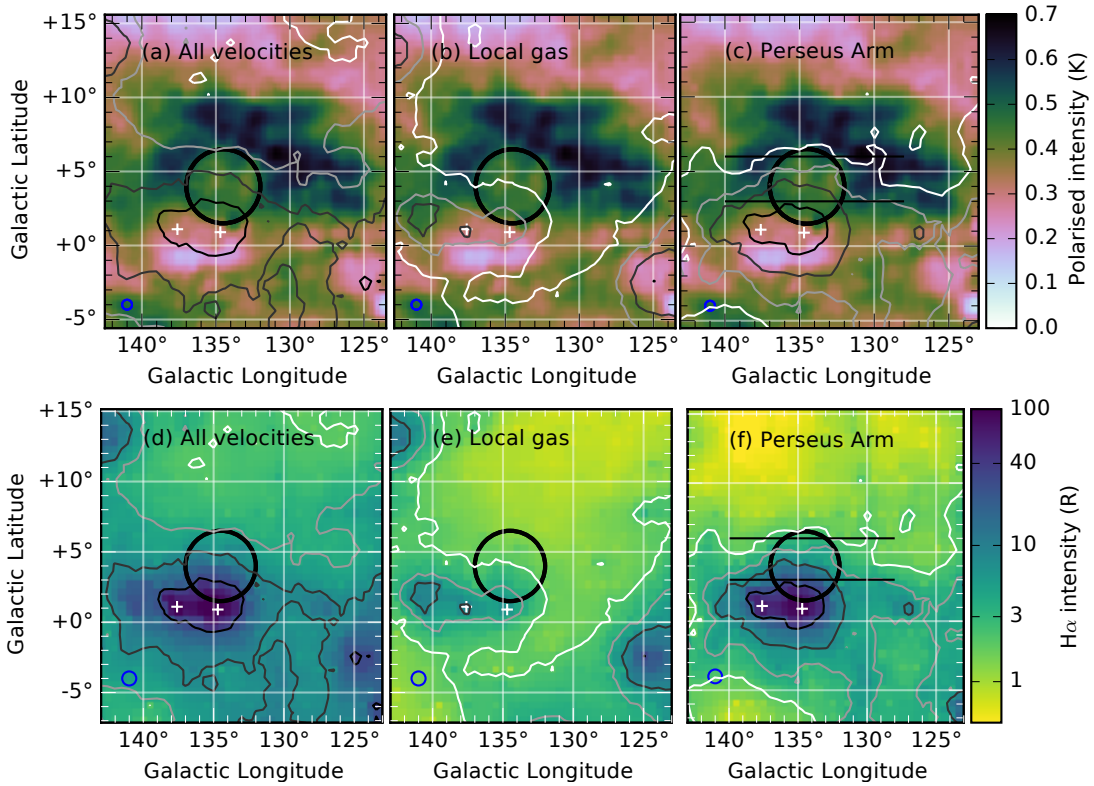

Figure 7. Top row: 1.5 GHz polarized continuum emission from GMIMS (as in Fig. 5*b*); we show the same map in all three columns. Bottom row: WHAM-SS Hα maps in three velocity ranges. Left: all velocities with significant emission (-75 km s^{-1} $< V_{\rm LSR} <$ $+15$ km s^{-1}). Middle: local velocities ($|V_{\rm LSR}| < 15$ km s^{-1}). Right: Perseus Arm velocities (-75 km s^{-1} $< V_{\rm LSR} <$ -30 km s^{-1}). Corresponding Hα contours at intensities of 2 (white), 4 (light gray), 8 (dark gray), and 32 R (black) are shown in both rows. White + signs show the centres of W4 and W5. Horizontal lines in panels *c* and *f* show the region used to calculate Fig. 8. Black circles are as in Fig. 5. 1.5 GHz data are shown with a linear scale; Hα data are shown with a logarithmic scale. The GMIMS (top) and WHAM (bottom) beams are shown with blue circles in the lower-left corner.

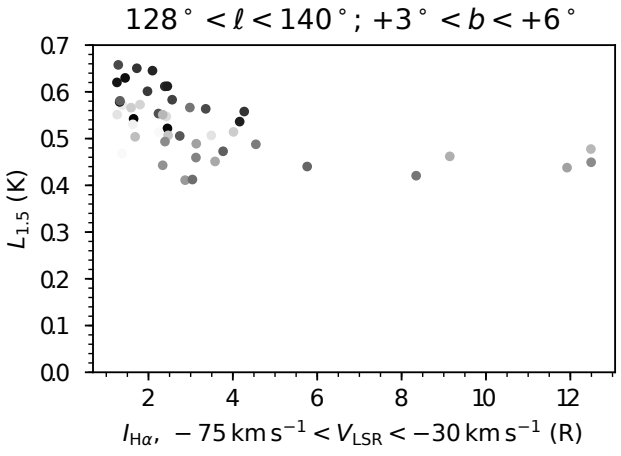

Figure 8. Polarized intensity ($L_{1.5}$) as a function of integrated Hα intensity from the Perseus Arm (-75 km s^{-1} $< V_{\rm LSR} <$ -30 km s^{-1}). Each point denotes $I_{\rm H\alpha}$ from a single WHAM beam compared to the average GMIMS $L_{1.5}$ within the beam in between the lines shown in Fig. 7. Points are colour-coded for Galactic longitude, with the lightest points at $\ell = 140°$ and black points at $\ell = 128°$.

resolved at arcminute resolution, evident in Figure 11 as a curved transition region from pink/white to green/black along $b = -1.5°$. We refer to this sharp edge as "the Smile"; it is probably a shock front. Morphological evidence suggests that the Smile is related to W4 and so is on the near side of the Perseus Arm, although attempts to associate the Smile with any observed kinematic features have failed (Landecker et al. 2010). In Figure 10, we trace the polarized intensity at $\ell \approx 135°$ as a function of b. We see that $L_{1.5} \approx 0.4$ K at $b < -2°$. At $b = -1.5°$, the polarized intensity drops abruptly to $L_{1.5} \approx 0.2$ K. The polarized intensity is similar from $-1.5° \lesssim b \lesssim -0.5°$ while the structured appearance we discuss above is evident in Figure 11. At $b \gtrsim -0.5°$, the W4 Hα and 2.7 GHz emission becomes significant and the polarized intensity increases to $L_{1.5} \approx 0.45$ K.

We interpret the region in front of W4 and the Smile as follows. W4 completely depolarizes all background emission by beam depolarization, even with the small CGPS beam. The observed ≈ 0.45 K emission in the direction of W4 is entirely from the foreground and is therefore smooth. The Smile is outside the H II region and provides a much lower column of ionized gas than W4. The depolarization in this region is therefore most likely Faraday screen depolarization within the Smile. Because the emission is more distant, it is more structured than the foreground emission observed in front of W4. This interpretation is supported by the fact that

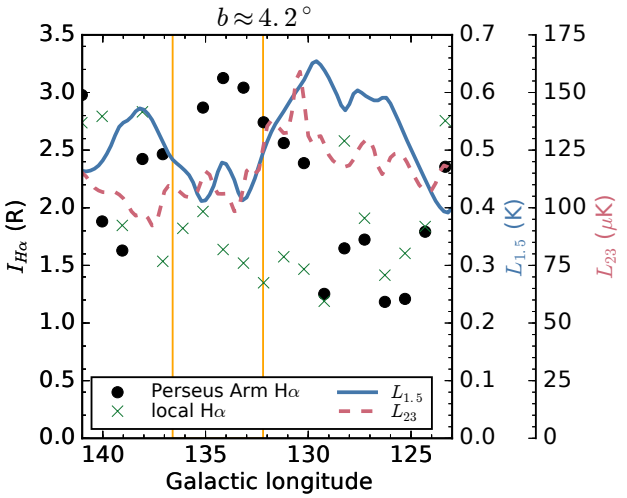

Figure 9. Polarized intensity ($L_{1.5}$ and L_{23}), Hα intensity at Perseus Arm velocities (-75 km s^{-1} $< V_{\rm LSR} < -30$ km s^{-1}), and Hα intensity at local velocities ($|V_{\rm LSR}| < 15$ km s^{-1}) as a function of Galactic longitude in the range $+4° \leq b \leq +5°$. The Hα points shown are from individual WHAM beams at $b = +4.2°$ because the WHAM survey is not Nyquist sampled. Vertical orange lines show the outer boundaries of the W4 superbubble walls from $I_{4.8}$ data (see Fig. 12 below).

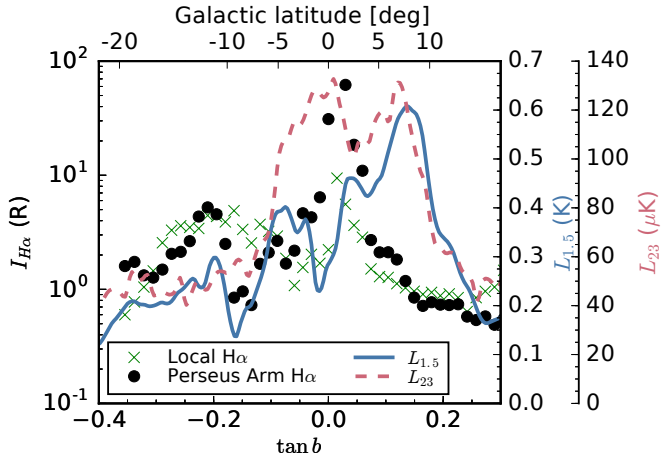

Figure 10. Vertical profiles of polarized intensity and Hα intensity (like Fig. 9), averaged over $133° < \ell < 136°$. Note that the Hα is shown on a logarithmic scale, while the polarized intensity is shown on linear scales.

there is no depolarization evident in the Smile at 23 GHz; if the Smile were geometrical depolarization, we would expect to see depolarization at 23 GHz.

Of particular interest is Sh2-202 around $(140°, +2°)$, diameter $170'$, at a distance of 0.97 ± 0.08 kpc (Foster & Brunt 2015). Wilkinson & Smith (1974) noted that this H II region does not depolarize emission at 610 MHz.[4] They took this as evidence that the Fan Region emission arises at a distance less than that of Sh2-202. In the CGPS data we see that Sh2-202 *does* leave an imprint on the 1.4 GHz polarized intensity image (Fig. 7 of Landecker et al. 2010), so at least some of the polarized emission must originate beyond the distance of Sh2-202. Again, the polarized emission across the face of Sh2-202 is smooth and probably local in origin, while that from its surroundings has the more typical mottled appearance that we identify with Perseus Arm emission.

Why can the influence of Sh2-202 as a Faraday screen be detected in the polarization image, when Sh2-202 is not a bright emitter in total intensity? The telescope is more sensitive to the Faraday rotation of a volume of ionized gas than to its bremsstrahlung in the presence of a typical interstellar magnetic field (Uyaniker et al. 2003). Based on the integrated Hα intensity of 37 R, we estimate $n_e = 1.6$ cm^{-3} in Sh2-202. Assuming a line-of-sight magnetic field of 2 μG, this yields $\phi \approx 100$ rad m^{-2}. This produces a Faraday rotation in the H II region at 1420 MHz of $\Delta\psi \approx 250°$, easily sufficient to cause Faraday screen depolarization.

These results from the CGPS seem at first sight to be incompatible with the results of Wilkinson & Smith (1974). However, their conclusions are based on a map of the Fan Region at 610 MHz. In Section 4.1, we showed that the appearance of the Fan Region below 1 GHz is quite different from that at 1.5 GHz and above, with the low-frequency emission associated entirely with a nearby feature.

4.4 Comparison to the W4 superbubble

Above W4 is the W4 "chimney" or superbubble (Normandeau et al. 1996). The superbubble walls are clearly seen in total intensity at 4.8 GHz ($I_{4.8}$). In Figure 12 we superimpose $I_{4.8}$ contours on the map of $L_{1.5}$. The $I_{4.8}$ contours fit inside the depression in $L_{1.5}$, strong evidence that the W4 superbubble is responsible for the depolarization feature centred at $(134.5°, +4°)$. The relative locations of the wall seen at 4.8 GHz and the peak of the 1.5 GHz polarized intensity are somewhat uncertain due to the lower angular resolution of the GMIMS data. The outer edges of the $I_{4.8}$ contours from the superbubble walls are shown as vertical orange lines in Figure 9. Again, it is clear that the $I_{4.8}$ superbubble walls are inside the region of low $L_{1.5}$. The gradient in $L_{1.5}$ as a function of longitude is much shallower than the gradient in $I_{4.8}$, likely at least partly due to the much lower angular resolution of the 1.5 GHz observations ($40'$ versus $9.5'$). However, the separation between the peak of $L_{1.4}$ and the edge of the $I_{4.8}$ wall is $\approx 2°$ on both sides of the superbubble, comfortably larger than the resolution of the 1.5 GHz observations. Therefore, the placement of the superbubble wall inside, not coincident with, the reduced $L_{1.5}$ emission does not appear to be a resolution effect. The total intensity maps at 1.4 GHz (West et al. 2007; Gao et al. 2015, hereafter GRR15) show that the compressed walls of the superbubble (seen at 4.8 GHz) lie inside a thicker envelope that is presumably ionized gas. The extent of this ionized material probably determines the extent of the depolarization seen in the GMIMS data. Since W4 is on the near side of the Perseus Arm, this is clear evidence that at least some of the Fan Region emission must be generated in the arm or beyond it.

[4] Note that there is a 10° error in the longitude scale of Figure 5 in Wilkinson & Smith (1974).

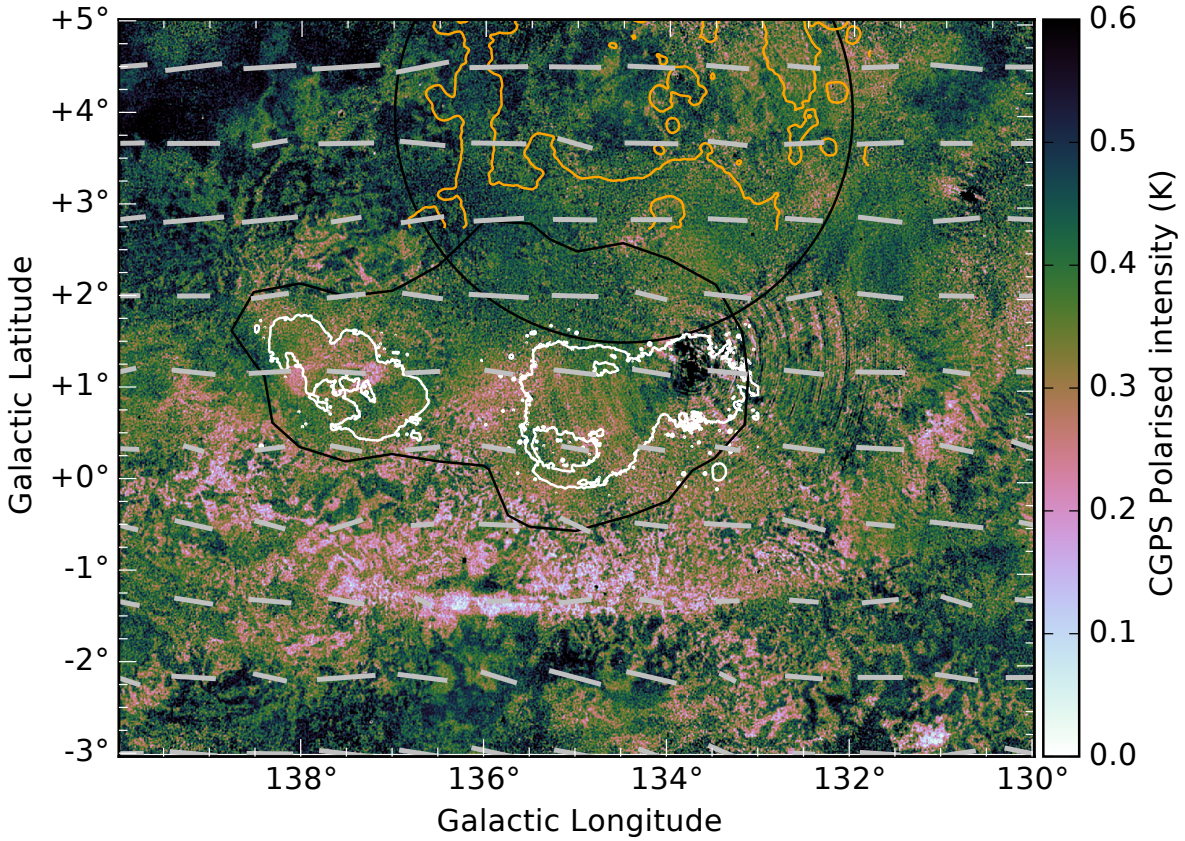

Figure 11. Polarized intensity at 1.4 GHz from the CGPS survey (Landecker et al. 2010). CGPS magnetic field vectors are overplotted, and white contours show the CGPS total intensity $I_{1.4}$ at 7.5 K. Orange contours show 4.8 GHz total power in the W4 superbubble from Gao et al. (2010, 2015). The black contour shows the WHAM-SS Hα intensity at Perseus Arm velocities at 32 R as in Fig. 7*c* and *f*. Note that the WHAM-SS data have a 1° resolution and were obtained on a 1° grid, so structure details on smaller scales are unreliable. The black circle is as in Figs. 5–7.

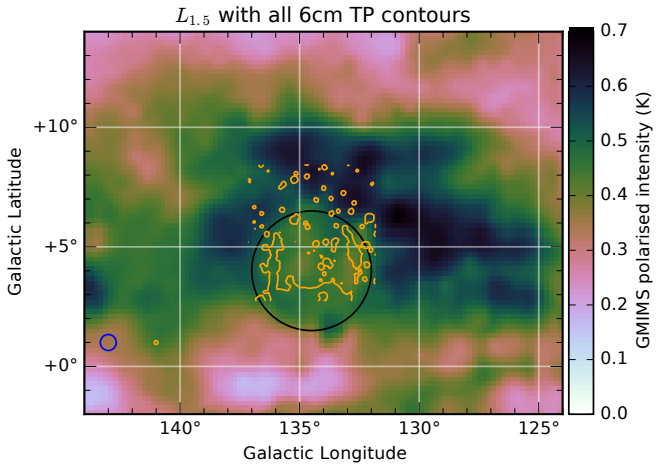

Figure 12. 1.5 GHz polarized continuum from GMIMS (as in Figs. 5*b* and 7) with orange contours of 4.8 GHz total power in the W4 superbubble region from Gao et al. (2010, 2015) (as in Fig. 11). The beams of the 1.5 GHz and 4.8 GHz observations are shown in blue and orange, respectively, in the lower-left corner.

GRR15 modeled the polarized emission along this line of sight accounting for depth depolarization due to the W4 superbubble. They modeled the superbubble as a shell structure with an inner radius of 65 pc and an outer radius of 72 pc. The shell walls are evident as vertical structures at $\ell \approx 136°$ and $\ell \approx 133°$ in Figure 12. The GMIMS beam is $\approx$ 23 pc at a distance of 2.0 kpc, so we do not resolve the shell wall. The West et al. (2007) DRAO Synthesis Telescope data (which lack zero-spacing data and thus are not sensitive to degree-scale structure) show depolarization of 0.025 K in the shell walls relative to the $\approx$ 0.5 K large-scale polarized brightness temperature at $\lambda = 21$ cm. In Figure 12, the shell walls are *inside* the edge of the 0.7 K Fan Region emission we see with GMIMS. GRR15 concluded that the depolarization by the shell walls is only $\approx 5\%$ at 21 cm.

Because the $\gtrsim 1°$-scale structure in the 1.4 GHz polarization images presented by GRR15 is tied to the Wolleben et al. (2006) survey (which does not show the large depolarization feature in the Fan Region, as we discussed in Section 4.1), the lack of the large depolarization feature in the data presented by GRR15 is expected. Our result is therefore not inconsistent with GRR15. The drop in intensity from the Fan Region outside the shell wall ($L_{1.5} \approx 0.7$ K) to inside the shell ($L_{1.5} \approx 0.5$ K) is evident with the GMIMS observations and indicates that the superbubble as a whole

depolarizes the Fan Region emission by $\approx 30\%$; this is the depolarization that is not evident in the GRR15 data. Then the superbubble wall depolarizes the 0.5 K 1.4 GHz emission on $\sim 10'$ scales by $\approx 5\%$; the GMIMS data are not sensitive to variations in intensity on angular scales this small.

5 DISCUSSION

5.1 Polarization fraction

The Fan Region has exceptionally high polarized intensity, but the Stokes I emission is typical of the surrounding parts of the Galaxy, $I_{1.5} \approx 1.6$ K. Equivalently, the polarization fraction in the Fan Region is unusually high, $\approx 40\%$ (Fig. 6). Aside from the North Polar Spur, no other region of the sky has such strong emission with such high fractional polarization. We have argued that $\gtrsim 30\%$ of the 1.5 GHz polarized emission originates in or beyond the Perseus Arm through a morphological comparison of $L_{1.5}$ to Hα and $I_{4.8}$ observations of ionized gas in the Perseus Arm (Sections 4.2 – 4.4). However, we can argue for the same conclusion from the polarized radio continuum data alone. Bingham & Shakeshaft (1967) were the first to do this, and their argument, using modern data, is as follows.

The maximum possible polarized fraction of synchrotron emission is 70% (Ginzburg & Syrovatskii 1965), so in the simplest model, $\sim 4/7$ of the radio continuum-emitting portion of the sightline contributes to the Fan Region signal. (That estimate must, of course, take into account the varying synchrotron emissivity along lines of sight through the Galaxy, as we do in Section 5.3.) Cosmic rays and magnetic fields, the ingredients which produce synchrotron emission, are well-distributed around the Galaxy, so the Stokes I emission is produced along a long (at least several kpc) path. If 4/7 of the path contributes to the polarized emission, the polarized emission must also be produced along a long path.

GRR15 applied the Sun et al. (2008) model of Galactic synchrotron emission to the W4 (and Fan Region) sightline. This model incorporates an enhanced synchrotron emissivity near the Sun (Fleishman & Tokarev 1995). Figure 5 of GRR15 shows that, in this model, $\approx 50\%$ of the Stokes I emission originates within 1 kpc of the Sun and $\approx 25\%$ originates within 500 pc. This figure describes the 4.8 GHz emission, but assuming that the spectral index is constant – which we expect for Stokes I, which does not suffer from Faraday depolarization – the same fractions should apply for $I_{1.5}$. If all of the Fan Region polarized emission that reaches our telescope originates within 500 pc (1 kpc) and the emitted fractional polarization is the maximal 70%, the expected polarization fraction is therefore 18% (35%). Therefore, the observed fractional polarization cannot be explained by emission within 500 pc of the Sun, and the fractional polarization in this model within 1 kpc of the Sun is still somewhat lower than (although probably within the uncertainties of) the observed fractional polarization.

5.2 Source of the synchrotron emission

What is the source of the emission? Synchrotron emission requires cosmic rays and a component of the magnetic field perpendicular to the line of sight. The scale heights of both cosmic rays and the regular component of the magnetic field are highly uncertain but of order a few kpc (Ferrière 2001), so there is no difficulty in finding the ingredients required to generate synchrotron emission at moderate latitudes. In addition to the morphological depolarization argument we presented in Section 4, there are then two lines of argument which suggest that a significant component of the emission is within the Perseus Arm or in the interarm region beyond the arm.

First, the Fan Region as seen at 1.5, 23, and 353 GHz extends from $b \approx -5^\circ$ to $b \approx +10^\circ$ (Section 4.2 and Figs. 4, 5, and 10), centred above the plane in a part of the Galaxy in which the emission beyond the Perseus Arm is warped upward to $b \approx +5^\circ$ (Section 3 and Fig. 3). If the warp explains the asymmetry of the Fan Region about the plane, some of the emission must be beyond the Perseus Arm.

Second, the magnetic field within the volume that generates the Fan emission must be uniform to produce the highly ordered polarization signal. In an interarm region the magnetic field is more likely to remain coherent over the long path length required to produce uniform synchrotron emission, and this may argue for at least a partial origin of the Fan Region emission in regions beyond the Perseus Arm. There is evidence for a more ordered field in interarm regions in the face-on spirals M51 and NGC 6946 (Beck 2007; Fletcher et al. 2011).

We therefore conclude that the most likely explanation for the Fan Region emission is geometric. The Fan Region is the portion of the Galaxy in which there is both a long path length with a coherent magnetic field, with a significant component perpendicular to the line of sight, and a warp which allows us to see much of the path length around depolarizing variations in the foreground gas. In the next subsection, we construct a simple model applying this qualitative discussion.

5.3 Spiral structure and synchrotron emission

A number of authors have constructed models of the Galactic magnetic field aiming to fit a number of observational constraints, including diffuse polarized emission. Some mask the Fan Region from their fits (e.g. Jansson & Farrar 2012), while others ignore it, leaving high residuals (e.g. Sun et al. 2008; Jaffe et al. 2010, 2011). In general, these models include a regular, planar field with a logarithmic spiral with a pitch angle of the same sign as the spiral defining the gaseous and stellar spiral structure[5] and a value of $8^\circ \lesssim \Theta \lesssim 12^\circ$. Van Eck et al. (2011) argue for an azimuthal field ($\Theta \approx 0^\circ$) in the outer Galaxy. The models also typically include turbulent, random, or striated fields; a vertical field; and contributions from discrete structures. Although these models have had varying degrees of success in matching the observed features in the Fan Region at low frequencies ($\nu \lesssim 2$ GHz), none have fit it with low residuals as a global feature. However, a spiral magnetic field with a positive pitch angle

[5] Jansson & Farrar (2012) define this pitch angle sign as positive, while Sun et al. (2008) define this sign as negative; we choose positive.

places the maximal polarized intensity in the second quadrant ($\ell < 180^\circ$) because the perpendicular component of the magnetic field is larger there than at $\ell = 180^\circ$ or in the third quadrant. Models developed in preparation for the Planck mission account for the 353 GHz polarized emission from the Fan Region with only a global spiral magnetic field and turbulence feature a maximum in polarization fraction around $\ell = 155^\circ$ (Fig. 7 of Miville-Deschênes et al. 2008), in the second quadrant though at a higher longitude than the Fan Region. These models too have high residuals in polarization in the Fan Region (Delabrouille et al. 2013; Planck Collaboration XIX 2015; Planck Collaboration XLII 2016).

We have attempted a very simple model which suggests one possible explanation while illustrating the problems that still need to be solved before an adequate, complete model of the Fan Region emission can be devised. Our model (inspired by Jansson & Farrar 2012 and Sun et al. 2008) includes only a radial variation in the magnetic field, excluding reversals (which are irrelevant to the calculation of synchrotron emissivity, which is proportional to $|\mathbf{B}|^2$), the vertical component of the field, and separate spiral arms. We assume that the magnetic field is

$$\mathbf{B} = \frac{B_0}{r_{\rm GC}}\,\hat{b}, \tag{2}$$

where $r_{\rm GC}$ is the distance from the Galactic Centre to the position, the unit vector along the logarithmic spiral defining the magnetic field is $\hat{b} = \sin(\Theta)\hat{r} + \cos(\Theta)\hat{\phi}$ in Galactocentric cylindrical coordinates, and the magnetic logarithmic spiral has a pitch angle Θ. We further assume that the cosmic ray electron density is (following Page et al. 2007)

$$n_{\rm cre} = n_{{\rm cre},0} e^{-r_{\rm GC}/h_r} {\rm sech}^2(z/h_z) \tag{3}$$

where $h_r = 5\,$kpc and $h_z = 1\,$kpc are the scale length and height of the cosmic ray electron distribution. At $r_{\rm GC} > 20\,$kpc, we set $\mathbf{B}$ and $n_{\rm cre}$ to zero. We model the thermal electron density outside the Solar circle as

$$n_e = n_1 \frac{{\rm sech}^2(r_{\rm GC}/A_1)}{{\rm sech}^2(r_\odot/A_1)} \exp\left(-\frac{|z|}{h_1}\right) + n_a {\rm sech}^2\left(\frac{z}{h_a}\right) e^{-(s_{\rm Per}/w_a)^2} {\rm sech}^2\left(\frac{r_{\rm GC}-r_\odot}{2.0\,{\rm kpc}}\right) \tag{4}$$

The first term is the smooth component of the Taylor & Cordes (1993) model of the Galactic electron density modified to use an exponential vertical distribution (Schnitzeler 2012). We choose $h_1 = 1.4\,$kpc and $h_1 n_1 = 0.022\,$kpc cm^{-3}, appropriate for the solar neighborhood (Gaensler et al. 2008; Savage & Wakker 2009), and $A_1 = 20\,$kpc. The second term represents the contribution from the Perseus spiral arm. We use the Reid et al. (2014) definition of the arm as a logarithmic spiral (Fig. 1); $s_{\rm Per}$ is the distance from a given position to the nearest point in the spiral arm, $n_a = 0.084$ cm^{-3} is the midplane electron density in the arm, and $w_a = 300$ pc is the assumed scale length of the electron density in the arm (Taylor & Cordes 1993).

For each longitude, we calculate the polarized synchrotron intensity from the polarization vector (Burn 1966; Sokoloff et al. 1998; O'Sullivan et al. 2012)

$$\mathcal{P} = \int_{\rm back}^{\rm observer} \varepsilon\, n_{\rm cre}(s)\, \left(\mathbf{B}(s) \times \hat{\mathbf{s}}\right)^2\, e^{2i\psi(s,\lambda)} ds \tag{5}$$

where the polarization angle is $\psi(s,\lambda) = \psi_0(s) + \phi(s)\lambda^2$ and

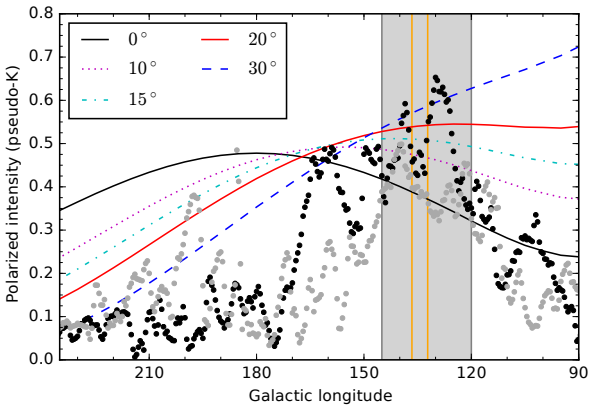

Figure 13. Synthetic polarized synchrotron intensity at $\lambda = 20$ cm as a function of longitude for a range of magnetic spiral pitch angles Θ as described in Section 5.3. This model includes depth and geometrical but not beam depolarization. As in Fig. 1, the longitude range of the Fan Region is shaded grey. We also show polarized intensity from GMIMS-HBN as a function of Galactic longitude at $b = +4.5^\circ$ (black dots) and $b = -4.5^\circ$ (light gray dots). The orange lines denote the outer edge of the W4 superbubble as in Fig. 9.

the Faraday depth is defined in equation (1). We use equations 2–4 to determine $n_{\rm cre}$, n_e, and $\mathbf{B}$. We choose the emissivity ε such that $n_{{\rm cre},0}\varepsilon = 0.7$ K cm^{-3} because this produces a synchrotron intensity in the Fan Region of ≈ 0.5 K, as observed, but the units of the output intensity can be scaled arbitrarily. We stay in the Galactic plane ($z = 0$). This implicitly but inexactly accounts for the warp: because the brightest 1.5 GHz emission in the Fan Region has a non-zero latitude ($b \approx +8^\circ$), the altitude probed by the sightline would increase with distance as $d \sin b$. In a warped disk, the latitude of the midplane increases with distance, so the distance between the sightline and the midplane is less than $d \sin b$. The inclusion of equations 1 and 4 accounts for depth depolarization and equation 5 includes geometrical depolarization, but we leave the inclusion of beam depolarization for Paper II because it involves a number of additional assumptions that are more difficult to quantify.

We show this modeled midplane polarized synchrotron intensity as a function of Galactic longitude in the outer Galaxy in Figure 13. The intensity is maximal at $\ell = 180^\circ$ for $\Theta = 0$ (a circular field). For non-zero pitch angles, the polarized synchrotron intensity is much higher in the second quadrant ($\ell < 180^\circ$) than in the third quadrant ($\ell > 180^\circ$) due to the small perpendicular component of $\mathbf{B}$ in the third quadrant. In the second quadrant, absent depth depolarization effects, the polarized synchrotron intensity is relatively flat as a function of longitude when $\Theta > 0$. However, due to depth depolarization, the observed polarized synchrotron intensity reaches a maximum and then decreases towards lower longitude. The longitude of the peak is lower for higher Θ; for $15^\circ \lesssim \Theta \lesssim 20^\circ$, the intensity peaks in the Fan Region. For $\Theta = 30^\circ$, the intensity does not peak in the second quadrant; it increases monotonically from $\ell = 180^\circ$ to $\ell = 90^\circ$.

We also show polarized intensity as a function of longitude in the entire portion of the outer Galaxy observed with

GMIMS-HBN in Figure 13. We show $L_{1.5}$ at $b = +4.5^\circ$, which runs through the centre of the Fan Region, and $b = -4.5^\circ$, which runs through the brightest polarized emission in the third quadrant (see Fig. 4*a*). The longitude of peak emission from the $\Theta \approx 20^\circ$ models roughly matches that in the observations. However, the observed polarized intensity falls off much more rapidly on either side of the peak than these models but more slowly than the $\Theta = 0^\circ$ model. In particular, the modeled $\Theta = 20^\circ$ polarized intensity is close to flat at $\ell < 130^\circ$.

The addition of a source of cosmic ray electrons concentrated around W4 can produce a peak in polarized intensity that roughly matches the observed cross-section through the Fan Region shown in Figure 13, but (a) there is no observational evidence, in the way of supernova remnants, for any source of high-energy electrons, and (b) this extra synchrotron emissivity would produce a peak in total intensity as well, which is not observed. The puzzling feature of the Fan Region is its exceptionally high polarized intensity, not its total intensity. The remaining difficulty is to explain the very high level of uniformity of the magnetic field implied by the high fractional polarization, and to explain that field regularity over the long path length that is implied by the observational evidence presented in this paper.

None of these simple models accurately match the morphology of the Fan Region. Models with a pitch angle $\Theta \approx 10^\circ$, as others have generally preferred (e.g. Sun et al. 2008; Miville-Deschênes et al. 2008; Jansson & Farrar 2012) produce a peak in intensity at higher longitudes than is observed in the Fan Region, while the steep pitch angle which best matches the longitude of peak intensity produces a higher intensity than is observed to lower longitudes than the Fan Region.

We conclude that it is unlikely that any simple model of the Galactic magnetic field will explain all of the observations. However, a spiral magnetic field with a relatively-steep pitch angle in the outer Galaxy can plausibly explain a distant origin of $\approx 30\%$ of the Fan Region emission. The Fan Region is in the quadrant of the Galaxy one would expect for a feature that arises due to synchrotron emission from the Galactic magnetic field with a spiral with a positive pitch angle. We note that the gas in the Outer Arm has a steep pitch angle, $\Theta = 18.6^\circ$ (Fig. 1 and Reid et al. 2014). It is possible that the Fan Region originates in a part of the Galaxy with a steeper pitch than is preferred at $r_{GC} \lesssim 10\,\mathrm{kpc}$, although this result is inconsistent with the azimuthal field toward the anticentre preferred by Van Eck et al. (2011) based on RM measurements of extragalactic sources.

6 SUMMARY AND CONCLUSIONS

We have used new GMIMS-HBN observations and other published observations to describe the morphology of polarized continuum emission found in data over $0.4-353$ GHz in the Fan Region. In summary, our key observational findings are:

(i) All-sky maps of 1.5, 23, and 353 GHz polarized emission from the Fan Region show that the Fan Region is roughly coincident with Hα emission from the Perseus Arm, especially the Hα emission from around the W3/W4/W5 complex of H II regions. They are similar in both location and angular extent on $\approx 10^\circ$ scales (Figs. 4 and 5*a*, *b*).

(ii) While the large-scale *extent* of the Fan Region polarized emission at > 1 GHz roughly coincides with the Perseus Arm Hα emission, the detailed structure on $\approx 1^\circ$ scales shows anticorrelation. A morphological comparison of GMIMS-HBN data at 1.5 GHz to Hα (Figs. 7 – 9 and Section 4.2) and radio continuum total intensity observations with high angular resolution (Figs. 11 and 12 and Section 4.3) shows that depolarization evident in polarized intensity is correlated with bright features in ionized gas related to the W4 star formation region and superbubble. The polarized intensity $L_{1.5}$ is 30% lower in regions with high integrated Hα intensity from the Perseus Arm ($I_{\mathrm{H}\alpha} > 5$ R) than in regions with low integrated Hα intensity from the Perseus Arm ($I_{\mathrm{H}\alpha} < 3$ R; Fig. 8).

(iii) At frequencies lower than 1.5 GHz, the size of the Fan Region decreases with decreasing frequency. At $\nu \lesssim 600$ MHz, the morphology of the Fan Region is quite different than at $\nu \gtrsim 1$ GHz: the low-frequency emission is a ring centred at $(137^\circ, +8^\circ)$, while the high-frequency emission extends to significantly lower longitudes ($\ell \approx 115^\circ$) and latitudes ($b \approx -5^\circ$) and does not have a ring-like component (Section 4.1 and Fig. 5).

(iv) The fractional polarization of the parts of the Fan Region with bright polarized emission at 1.5 GHz is high, $L_{1.5}/I_{1.5} \approx 40\%$ (Section 4.1 and Fig. 6).

Observational fact (ii) leads us to conclude that at least 30% of the 1.5 GHz polarized continuum emission seen in the brightest parts of the Fan Region originates in or beyond the Perseus Arm. If the Perseus Arm acts as a Burn (1966) slab which depolarizes all background emission – a conclusion supported by the smoothness of the CGPS data – most or all of the remaining $\approx 70\%$ would originate in front of the Perseus Arm. Observational fact (iii) suggests that this high-frequency structure is different in physical origin than most of the low-frequency ($\nu \lesssim 600$ MHz) emission that was first associated in the literature with the Fan Region. The more distant high-frequency emission is likely more depolarized at low frequencies (which we will discuss more in Paper II), so the emission and Faraday effects in local features, within about 500 pc, may dominate. These local features appear to make an insignificant contribution to the Fan Region at high frequencies. The rest of our conclusions apply to the $\nu > 1$ GHz data.

Observational fact (iv) implies that the entire line of sight must be involved in generating the Fan Region synchrotron emission (Section 5.2). Even though a majority (up to 70%) of the 1.5 GHz emission could originate in front of the Perseus Arm, it seems highly unlikely that most of the foreground emission is within ≈ 500 pc while 30% of the emission originates in or beyond the Perseus Arm. It is far more plausible that the origin of the Fan Region is not a discrete, local structure. Therefore, the Fan Region must be a very large phenomenon, several kpc in extent, which we can only explain as a consequence of Galactic structure and geometry. We cannot confine it, as most previous authors have done, to the nearest 500 pc.

We could have reached many of our conclusions about the distance of the Fan Region without the GMIMS data or the Hα data based entirely on the high fractional polar-

ization, the modelling of Section 5.3, and the evidence from the *Planck* 353 GHz data, together with the modelling done by the Planck consortium (see references in Section 5.3). The GMIMS and WHAM data, taken together, reinforce our conclusion.

Our determination of the distance to the Fan Region emission from the GMIMS and WHAM data is strongly supported by the correlation of the $\approx 4^\circ$-diameter region of reduced polarized intensity around $(134.5^\circ, +4^\circ)$ with Hα intensity at Perseus Arm velocities and the W4 superbubble. This is a relatively small patch of sky. Our extrapolation from the Fan Region to an analysis of the Galactic magnetic field rests on analysis of observations over much larger scales, the fact that the polarized intensity is much higher in the second quadrant (where the Fan Region extends over $\sim 60^\circ$) than in the third quadrant.

We suggest three ideas which explain some of the observed features of the Fan Region emission:

(i) A spiral magnetic field with a steep pitch angle ($\Theta \approx 15^\circ - 20^\circ$) moves the longitude of peak emission to $\ell \approx 130^\circ$, in the Fan Region (Fig. 13). However, the increase in intensity is less sharp than observed, and the pitch angle is significantly steeper than the $\Theta \approx 10^\circ$ preferred by most existing models.

(ii) An increase in the synchrotron emissivity associated with W4 could be scaled to produce the observed Fan Region intensity. Qualitatively, this is consistent with the morphology of the brightest emission from the Fan Region, surrounding W4. However, the $60^\circ \times 30^\circ$ extent of the Fan Region is much larger than W4 itself. Moreover, it is not obvious how to increase the polarized intensity without also increasing the total intensity, and it is also not obvious how increased intensity in a presumably-turbulent region associated with star formation could produce such regular polarization vectors and such a high polarization fraction. This idea also does not explain the offset of the Fan Region above $b = 0^\circ$.

(iii) Due to the warp, distant ($d > 2\,\mathrm{kpc}$) portions of this part of the Galaxy are centred at $b = +3^\circ$ to $+9^\circ$ (Fig. 3). Moreover, the pitch of the gaseous arms is considerably steeper in the outer Galaxy (Fig. 1); because most models of the magnetic field are not constrained so far out ($R \gtrsim 20\,\mathrm{kpc}$), a steeper pitch angle may be consistent with existing models. It is not clear that the cosmic ray electron density is high enough in the outer Galaxy, where there is little star formation, to produce the observed synchrotron intensity. However, in M51, there is detectable polarized emission at 1.4 GHz out to $\sim 50\,\mathrm{kpc}$ from the galactic centre, well beyond the optical spiral arms (Fletcher et al. 2011).

None of these three ideas explain all of the observed features of the Fan Region, so the origin of the Fan Region remains puzzling. We conclude that $\approx 30\%$ of the integrated 1.5 GHz Fan Region emission is depolarized by ionized gas in the Perseus Arm, suggesting that it is a puzzling Galactic-scale feature, not a relatively-small, purely local feature. This result suggests that future detailed models of the Galactic magnetic field should attempt to fit the Fan Region with the prior that the emission originates along a long path length or at a large distance, perhaps incorporating the warp or a spiral magnetic field with a large pitch angle in at least part of the Galaxy.

ACKNOWLEDGEMENTS

ASH acknowledges useful discussions with R. A. Benjamin and V. Jelic. TLL acknowledges useful discussions with T. Foster and J. C. Brown. We thank two referees for comments which strengthened the paper.

This research made use of APLpy[6] and Astropy (Astropy Collaboration et al. 2013).

The Wisconsin H-Alpha Mapper is funded by the US National Science Foundation. The Dominion Radio Astrophysical Observatory is operated as a National Facility by the National Research Council Canada. ASH was partially supported by NSF grant AST-1442650. KD and MW were supported by the Natural Sciences and Engineering Research Council of Canada. BMG acknowledges the support of the Australian Research Council through grant FL100100114. The Dunlap Institute is funded through an endowment established by the David Dunlap family and the University of Toronto. NMM-G acknowledges the support of the Australian Research Council through Future Fellowship FT150100024. MH acknowledges the support of research program 639.042.915, which is partly financed by the Netherlands Organization for Scientific Research (NWO).

REFERENCES

Astropy Collaboration et al., 2013, A&A, 558, 33
Baars J. W. M., Genzel R., Pauliny-Toth I. I. K., Witzel A., 1977, A&A, 61, 99
Beck R., 2007, A&A, 470, 539
Benjamin R. A., 2008, ASPC, 387, 375
Bennett C. L., et al., 2013, ApJS, 208, 20
Berkhuijsen E. M., Brouw W. N., Muller C. A., Tinbergen J., 1964, BAN, 17, 465
Bernardi G., et al., 2009, A&A, 500, 965
Bingham R. G., Shakeshaft J. R., 1967, MNRAS, 136, 347
Brentjens M. A., de Bruyn A. G., 2005, A&A, 441, 1217
Brouw W. N., Spoelstra T. A. T., 1976, A&AS, 26, 129
Burn B. J., 1966, MNRAS, 133, 67
Calabretta M. R., Greisen E. W., 2002, A&A, 395, 1077
Carretti E., Bernardi G., Sault R. J., Cortiglioni S., Poppi S., 2005, MNRAS, 358, 1
Churchwell E., et al., 2009, PASP, 121, 213
Delabrouille J., et al., 2013, A&A, 553, 96
Du X., Landecker T. L., Robishaw T., Gray A. D., Douglas K. A., Wolleben M., 2016, PASP, 128, 115006
Ferrière K. M., 2001, RvMPh, 73, 1031
Fleishman G. D., Tokarev Y. V., 1995, A&A, 293, 565
Fletcher A., Beck R., Shukurov A., Berkhuijsen E. M., Horellou C., 2011, MNRAS, 412, 2396
Foster T., Brunt C. M., 2015, AJ, 150, 147
Foster T., MacWilliams J., 2006, ApJ, 644, 214
Gaensler B. M., Dickey J. M., McClure-Griffiths N. M., Green A. J., Wieringa M. H., Haynes R. F., 2001, ApJ, 549, 959
Gaensler B. M., Madsen G. J., Chatterjee S., Mao S. A., 2008, PASA, 25, 184
Gao X. Y., et al., 2010, A&A, 515, 64
Gao X. Y., Reich W., Reich P., Han J. L., Kothes R., 2015, A&A, 578, A24
Ginzburg V. L., Syrovatskii S. I., 1965, ARA&A, 3, 297
Gray A. D., Landecker T. L., Dewdney P. E., Taylor A. R., 1998, Nature, 393, 660

[6] http://aplpy.github.com

Gray A. D., Landecker T. L., Dewdney P. E., Taylor A. R., Willis A. G., Normandeau M., 1999, ApJ, 514, 221
Green D. A., 1989, AJ, 98, 2210
Hachisuka K., Brunthaler A., Menten K. M., Reid M. J., Hagiwara Y., Mochizuki N., 2009, ApJ, 696, 1981
Haffner L. M., Reynolds R. J., Tufte S. L., 1999, ApJ, 523, 223
Haffner L. M., Reynolds R. J., Tufte S. L., Madsen G. J., Jaehnig K. P., Percival J. W., 2003, ApJS, 149, 405
Haffner L. M., Reynolds R. J., Madsen G. J., Hill A. S., Barger K. A., Jaehnig K. P., Mierkiewicz E. J., Percival J. W., 2010, BAAS, 215, 265
Haverkorn M., Katgert P., de Bruyn A. G., 2003, A&A, 404, 233
Heald G. H., 2009, Cosmic Magnetic Fields: From Planets, 259, 591
Iacobelli M., Haverkorn M., Katgert P., 2013a, A&A, 549, 56
Iacobelli M., et al., 2013b, A&A, 558, 72
Jaffe T. R., Leahy J. P., Banday A. J., Leach S. M., Lowe S. R., Wilkinson A., 2010, MNRAS, 401, 1013
Jaffe T. R., Banday A. J., Leahy J. P., Leach S., Strong A. W., 2011, MNRAS, 416, 1152
Jansson R., Farrar G. R., 2012, ApJ, 757, 14
Kalberla P. M. W., Burton W. B., Hartmann D., Arnal E. M., Bajaja E., Morras R., Pöppel W. G. L., 2005, A&A, 440, 775
Kalberla P. M. W., Dedes L., Kerp J., Haud U., 2007, A&A, 469, 511
Kang J.-h., Koo B.-C., Salter C., 2012, AJ, 143, 75
Kennicutt R. C., Evans N. J., 2012, ARA&A, 50, 531
Landecker T. L., et al., 2010, A&A, 520, 80
Madsen G. J., Reynolds R. J., 2005, ApJ, 630, 925
Madsen G. J., Reynolds R. J., Haffner L. M., 2006, ApJ, 652, 401
Miville-Deschênes M. A., Ysard N., Lavabre A., Ponthieu N., Macías-Pérez J. F., Aumont J., Bernard J. P., 2008, A&A, 490, 1093
Normandeau M., Taylor A. R., Dewdney P. E., 1996, Nature, 380, 687
O'Sullivan S. P., et al., 2012, MNRAS, 421, 3300
Page L., et al., 2007, ApJS, 170, 335
Planck Collaboration XIX, 2015, A&A, 576, A104
Planck Collaboration I, 2016, A&A, 594, A1
Planck Collaboration XLII, 2016, A&A, 596, A103
Reich W., 1982, A&AS, 48, 219
Reich P., Reich W., 1986, A&AS, 63, 205
Reich P., Testori J. C., Reich W., 2001, A&A, 376, 861
Reid M. J., et al., 2009, ApJ, 700, 137
Reid M. J., et al., 2014, ApJ, 783, 130
Savage B. D., Wakker B. P., 2009, ApJ, 702, 1472
Schnitzeler D. H. F. M., 2012, MNRAS, 427, 664
Schnitzeler D. H. F. M., Katgert P., de Bruyn A. G., 2009, A&A, 494, 611
Sokoloff D. D., Bykov A. A., Shukurov A., Berkhuijsen E. M., Beck R., Poezd A. D., 1998, MNRAS, 299, 189
Spoelstra T. A. T., 1984, A&A, 135, 238
Sun X. H., Han J. L., Reich W., Reich P., Shi W. B., Wielebinski R., Fürst E. J., 2007, A&A, 463, 993
Sun X. H., Reich W., Waelkens A., Enßlin T. A., 2008, A&A, 477, 573
Sun X. H., et al., 2015, ApJ, 811, 40
Tauber J. A., et al., 2010, A&A, 520, A1
Taylor J. H., Cordes J. M., 1993, ApJ, 411, 674
Taylor A. R., et al., 2003, AJ, 125, 3145
Tribble P. C., 1991, MNRAS, 250, 726
Uyaniker B., Landecker T. L., Gray A. D., Kothes R., 2003, ApJ, 585, 785
Van Eck C. L., et al., 2011, ApJ, 728, 97
Verschuur G. L., 1968, Obs, 88, 15
West J. L., English J., Normandeau M., Landecker T. L., 2007, ApJ, 656, 914
Westerhout G., Seeger C. L., Brouw W. N., Tinbergen J., 1962, BAN, 16, 187
Wielebinski R., Shakeshaft J. R., Pauliny-Toth I. I. K., 1962, Obs, 82, 158
Wilkinson A., Smith F. G., 1974, MNRAS, 167, 593
Wolleben M., 2005, PhD thesis, Universität Bonn, Max-Planck-Institut für Radioastronomie, Auf dem ügel 69, Bonn, Germany
Wolleben M., Landecker T. L., Reich W., Wielebinski R., 2006, A&A, 448, 411
Wolleben M., et al., 2009, in Strassmeier K. G., Kosovichev A. G., Beckman J. E., eds, Cosmic Magnetic Fields: From Planets. Cambridge University Press, pp 89–90
Wolleben M., Landecker T. L., Hovey G. J., Messing R., Davison O. S., House N. L., Somaratne K. H. M. S., Tashev I., 2010a, AJ, 139, 1681
Wolleben M., et al., 2010b, ApJ, 724, L48
Xu Y., Reid M. J., Zheng X. W., Menten K. M., 2006, Science, 311, 54

This paper has been typeset from a TEX/LATEX file prepared by the author.